


12-2016

Investigation of the Optical Properties of PbSe/ PbX Nanocrystals for Photodetector Applications

Haley Ann Morris

University of Arkansas, Fayetteville

Follow this and additional works at: <http://scholarworks.uark.edu/etd>

 Part of the [Electromagnetics and Photonics Commons](#), [Electronic Devices and Semiconductor Manufacturing Commons](#), and the [Semiconductor and Optical Materials Commons](#)

Recommended Citation

Morris, Haley Ann, "Investigation of the Optical Properties of PbSe/PbX Nanocrystals for Photodetector Applications" (2016). *Theses and Dissertations*. 1828.

<http://scholarworks.uark.edu/etd/1828>

This Thesis is brought to you for free and open access by ScholarWorks@UARK. It has been accepted for inclusion in Theses and Dissertations by an authorized administrator of ScholarWorks@UARK. For more information, please contact scholar@uark.edu, ccmiddle@uark.edu.

Investigation of the Optical Properties of PbSe/PbX Nanocrystals for Photodetector Applications

A thesis submitted in partial fulfillment
of the requirements for the degree of
Master of Science in Microelectronics-Photonics

by

Haley Ann Morris
Arkansas Tech University
Bachelor of Science in Physics, 2014
Arkansas Tech University
Bachelor of Science in Mathematics, 2014

December 2016
University of Arkansas

This thesis is approved for recommendation to the Graduate Council.

Dr. Omar Manasreh
Thesis Director

Dr. William F. Oliver III
Committee Member

Dr. Jingxian Wu
Committee Member

Dr. Rick Wise
Ex-Officio Member

The following signatories attest that all software used in this thesis was legally licensed for use by Haley Ann Morris for research purposes and publication.

Ms. Haley Ann Morris, Student Dr. Omar Manasreh, Thesis Director

This thesis was submitted to <http://www.turnitin.com> for plagiarism review by the TurnItIn company's software. The signatories have examined the report on this thesis that was returned by TurnItIn and attest that, in their opinion, the items highlighted by the software are incidental to common usage and are not plagiarized material.

Dr. Rick Wise, Program Director Dr. Omar Manasreh, Thesis Director

Abstract

Lead selenide and lead selenide/lead sulfide core/shell nanocrystals were investigated for use in near infrared photodetectors. A colloidal synthesis method was used for both the core and core/shell configurations. The lead sulfide shell was examined in order to mitigate oxidation of the nanoparticle surface. Absorbance and photoluminescence spectra were measured at room temperature and 77 K, respectively. Transmission electron microscopy images were also obtained to confirm crystallography and size. Bulk lead selenide was simulated in WIEN2k utilizing the linear-augmented plane wave method of solving density functional theory to better understand the electronic structure of PbSe. The crystal structure, electron density, band structure and density of states are presented and discussed. The calculations correctly predicted a direct band gap at the L point in the Brillouin zone. The band gap calculated was 0.40 eV.

Acknowledgements

I would like to acknowledge my colleagues, especially Yahia Makableh, Ahmad Nusir, Ramesh Vasan and Juan Aguilar, in my research group for their help and guidance throughout my time here at the University of Arkansas. The resources and insight provided by Dr. Omar Manasreh during the course of my research here has been instrumental in my success. I also appreciate his instruction in the practice of technical writing, which was very helpful in this literary endeavor. I would also like to thank Dr. Bothina Manasreh for her much needed help in operating the program package used for the simulation, and her considerate reassurance.

I would also like to recognize Dr. Benamara for his assistance in obtaining and interpreting the TEM measurements. A special thanks to Renee Hearon for her support and encouragement throughout my graduate experience. I would like to acknowledge Dr. Rick Wise for his advice concerning my education and career opportunities. I would also like to thank Justin Hill for his support and friendship during my time as a graduate student.

Dedication

This thesis is dedicated to my family and friends who supported me throughout the process. I thank my parents, who never doubted that I would be successful in my endeavors, and Josh, who always encouraged, fortified and calmed me when I needed it most.

Table of Contents

Chapter 1 Introduction	1
1.1 Motivation.....	1
1.2 Background.....	4
1.2.1 Nanostructures	4
1.2.2 Pb Compounds.....	9
Chapter 2 Experimental Methods	13
2.1 Colloidal Synthesis	13
2.1.1 PbSe Synthesis Procedure.....	15
2.1.2 PbSe/PbS Synthesis Procedure	16
2.1.3 PbSe/PbSe _x S _{1-x} Synthesis Procedure.....	16
2.2 Characterization Techniques.....	17
2.3 Simulation Techniques	21
Chapter 3 Results and Discussion.....	23
3.1 Simulation Results	23
3.2 Experimental Results	29
3.2.1 PbSe	30
3.2.2 PbSe/PbS.....	37
3.2.3 PbSe/PbSe _x S _{1-x}	45
Chapter 4 Conclusion.....	46
Appendix A: Description of Research for Popular Publication.....	52
Appendix B: Executive Summary of Newly Created Intellectual Property	54
Appendix C: Potential Patent and Commercialization Aspects of listed Intellectual Property Items.....	55
Appendix D: Broader Impact of Research.....	56
D.1 Applicability of Research Methods to Other Problems	56
D.2 Impact of Research Results on U.S. and Global Society.....	56
D.3 Impact of Research Results on the Environment.....	56
Appendix E: Microsoft Project for MS MicroEP Degree Plan.....	58
Appendix F: Identification of All Software Used in Research and Thesis Generation	59

Appendix G: All Publications Published, Submitted and Planned 60

List of Figures

Figure 1.1. The electronic density of states as a function of energy for four different configurations: zero, one, two, and three dimensional.	5
Figure 1.2. The band diagrams of bulk and quantum structures are shown with the interband and intersubband transitions labeled.	6
Figure 1.3 A schematic shows how the composition of the nanocrystals changes the band structure of the material [27].	8
Figure 1.4. The crystal structure of PbSe is zinc blende.	10
Figure 1.5. The band diagram for PbSe and PbS is shown with energy in eV.	12
Figure 2.1. The picture of the set up used for all synthesis procedures was taken during synthesis on 04/28/2016 by Haley Morris.	14
Figure 2.2. A cubic lattice is presented with the dashed lines representing different planes. The differing interplanar distances are labeled for the two orientations depicted.	20
Figure 2.3. The schematic depicts how a material is divided into spherical muffin tins, modeled by linear combinations of radial wavefunctions, and the remaining space is the interstitial region which is modeled by plane waves.	21
Figure 3.1. The crystal structure of PbSe is rock salt. Two different angles of the material are shown and were generated using WIEN2k and XCrysDen.	23
Figure 3.2. The volume optimization curve is plotted as total energy in Rydberg vs. volume in cubic angstroms.	24
Figure 3.3. The full band diagram for bulk PbSe shows the direct band gap of 0.40 eV found at the L point.	26
Figure 3.4. The electron density was calculated in WIEN2k. The lead and selenium atoms are labeled.	27
Figure 3.5. The contributions to the density of states of PbSe were calculated and plotted as a function of energy. (a) The total density of states for PbSe as well as the lead and selenium contributions. (b) The Pb contribution to the density of states and its orbital contributions: s, p and d.	298
Figure 3.5., cont'd. (c) The Se contribution to the density of states was divided between the s, p and d orbitals.	29

Figure 3.6. The absorbance spectra at room temperature of PbSe nanocrystals with four different growth times dispersed in either chloroform or hexane is plotted in (a). An enlarged plot of the first excitonic peak is shown in (b).....	31
Figure 3.7. Image (a) is a TEM image of the PbSe nanocrystals grown at 140 °C for 20 seconds. Image (b) is a close up of image (a) with the average measured interatomic distance of 3.34 Å labeled. Image (c) is a FFT of image (a) consisting of multiple nanocrystals. In image (d), a FFT was performed in ImageJ on image (b), a single nanocrystal.	33
Figure 3.8. The gray value of each pixel along a bisecting line of the nanocrystal is presented as a function of distance in nanometers. The PbSe TEM inset displays the cross-section measured as a yellow line. The interatomic spacing is 3.33 Å.	34
Figure 3.9 Energy-dispersive X-ray spectroscopy results for PbSe nanocrystals.	35
Figure 3.10. The absorbance spectrum measured at room temperature and photoluminescence spectrum measured at 77 K as a function of wavelength were obtained for PbSe nanocrystals. The inset is a TEM image.	36
Figure 3.11 The absorbance spectra measured at room temperature as function of wavelength were obtained for PbSe/PbS nanocrystals of different sizes, as shown in (a). The spectra of the samples with differing growth times injected at 180 °C were isolated in (b).....	39
Figure 3.11. cont'd. The spectra for nanocrystals with differing injection temperatures, all grown for 15 minutes, are plotted in (c).	40
Figure 3.12. Part (a) is a TEM image of the PbSe/PbS nanocrystals grown at 180°C for 15 minutes. Image (b) is a close up of a single nanocrystal in (a), with the average measured interatomic spacing illustrated. The FFT shown in (c) is a transform of (a) . Part (d) is a FFT of image (b).	41
Figure 3.13. The gray value of each pixel along the yellow line seen in the inset TEM image was plotted as a function of distance.	42
Figure 3.14. The EDX measurements of the PbSe/PbS core/shell nanocrystals are shown with each peak labeled with the corresponding element.....	43
Figure 3.15. The absorbance and photoluminescence spectra as a function of wavelength for PbSe/PbS nanocrystals were measured at 300 K and 77 K, respectively. The inset is a TEM image.	44
Figure 3.16. The absorbance measurement of the alloyed shell nanocrystals revealed no discrete transitions.	45

List of Tables

Table 1.1. The band gap (at room temperature) in eV, exciton Bohr radius in nm, and the effective mass for holes and electrons are listed for the three main lead salt compounds [17].	11
--	----

Chapter 1 Introduction

1.1 Motivation

As the world's population and the use of technology grows, the demand for energy is increasing at an accelerated rate. Renewable energy, such as wind, solar and thermal energy, is the ideal long-term solution. The federal government has several initiatives to encourage the growth of this sector over the coming decades. Outlined in the 2013 Climate Action Plan [1], these goals include increasing the number of alternative energy facilities, updating our nation's energy infrastructure and funding research focused on relieving the strain that pollution puts on the environment. Research into alternative energy is also necessary to increase the prominence of renewable resources in the energy sector. Investigation in the field is focused on ways to improve the efficiency and reduce the production cost of these devices. These objectives are important because in order to move away from fossil fuels, alternative energy must be financially advantageous.

With this intention, research into photovoltaics has grown and diversified. Novel materials and devices incorporating nanostructures have yielded improvements in both efficiency and cost. However, the maximum theoretical efficiencies have not yet been met [2]. Thermoelectric devices are also of interest due to their potential to harvest waste heat. They can be used in cars, power plants and spacecraft to absorb excessive heat and convert it to usable electricity. NASA utilized radioisotope thermoelectric generators for several missions including Voyager 1 and 2, Cassini, and Pioneer 10 and 11 [3]. One way to advance photovoltaic and

thermoelectric devices is to improve the material properties. This can be done through changing the material composition, structure, and size.

In previous decades, nanostructures have received concentrated research focus due to their unique properties. Different nanostructures include nanorods, nanowires and quantum dots. Nanoparticles exhibit discrete energy levels due to the quantum size effect. Carriers are spatially confined in these nano-scale structures, yielding unique properties drastically different from the corresponding bulk material. This allows band gap engineering through size adjustments of the nanoparticles. The nanostructures can then be made to operate within a specific range for specific applications. The synthesis of nanoparticles can be achieved with a solution based synthesis method which is lower in cost than vacuum based methods, such as chemical vapor deposition (CVD), metal organic chemical vapor deposition (MOCVD) and molecular beam epitaxy (MBE). Solution based synthesis methods can be scaled up to achieve the mass quantities needed for commercial use more easily than vacuum techniques.

Group IV-VI semiconductors have been investigated for use in biomarkers, photovoltaic and thermoelectric devices. The compounds PbSe and PbS have been studied extensively due to their narrow band gap. Nanostructures composed of these compounds reveal distinctive properties that make them attractive for device applications. Specifically, the large Bohr exciton radius found in these materials allow access to the extreme quantum confinement regime. Also, these materials operate in the near-infrared to visible range. The IR spectrum is technically important in applications. Infrared light is crucial to optical communication, solar power, and some biomedical imaging and therapy. Improvements in materials that operate in this range would affect a wide variety of technical fields, such as communications, medical imaging, and photovoltaics. The potential of these materials continues to drive research in this field.

Lead chalcogenide nanocrystals, which include PbSe and PbS, offer unique properties that have yet to be fully understood. Computational simulations offer a relatively inexpensive way to explore material properties of novel nanostructures. This work will further the knowledge of these materials through both experimental study and theoretical simulation of PbSe. WIEN2k is a powerful simulation tool to investigate the properties of nanostructures. Expanding knowledge of lead chalcogenides through study of the structural, electrical and optical properties would lead to improvements in various fields due to the prevalent use of these materials. The efficiency of photovoltaic and thermoelectric devices would improve and thus become more viable in the marketplace.

The further development and understanding of materials is necessary for the advancement of technology. Lead chalcogenides specifically have the potential to improve upon existing alternative energy harvesting methods. This can improve the efficiency of photovoltaic and thermoelectric devices which is important for the adoption of alternative energy on a large scale. Also, the solution-based synthesis process is an inexpensive and easily scalable process. This and increased efficiency are two factors that contribute to moving away from fossil fuels to more environmentally friendly energy sources. Alternative energy must be financially advantageous in order for the free market to make the major transition away from fossil fuels that is needed. As a society, moving towards alternative energy is a necessary change. The current use of fossil fuels is responsible for pollutants that are damaging to the environment. Making the transformation to renewable resources would reduce output of pollutants, and thereby reduce the damage to ecosystems. Another advantage is that renewable resources will never be exhausted. This is an industry that will only grow in the long-term and is well worth the investment. It would also create high-tech jobs to sustain and grow this budding industry.

1.2 Background

The prevalence of nanostructures has grown in recent decades. The applications of nanostructures spans solar cell design [4]–[8], light emitting diodes [9]–[11], thermoelectric devices [12]–[15], surface coatings [16]–[20], and biomedical applications (including imaging, cancer treatment, and drug delivery) [21]–[25]. The size-tunable band gap of nanostructures provides a level of control over material properties, and thus is quite attractive for many applications.

1.2.1 Nanostructures

Semiconductor nanostructures are a topic of interest due to their unique properties and advantages over three dimensional, or bulk, materials. There are three main types of nanostructures: quantum wells, quantum wires, and quantum dots. Quantum wells are dubbed a two dimensional system due to fact that the material, when bound in a plane, has only two degrees of freedom. Quantum wires, or nanowires, have one degree of freedom and are therefore considered a one dimensional system. Bound in all three dimensions, quantum dots are zero dimensional. The reduction in the degree of freedom has an effect on the distribution of the density of states, which is the number of states per unit energy [26]. Figure 1.1 illustrates the density of states as a function of energy for three, two, one, and zero dimensional nanostructures. As the degree of spatial confinement increases, the density of states becomes discretized rather than continuous.

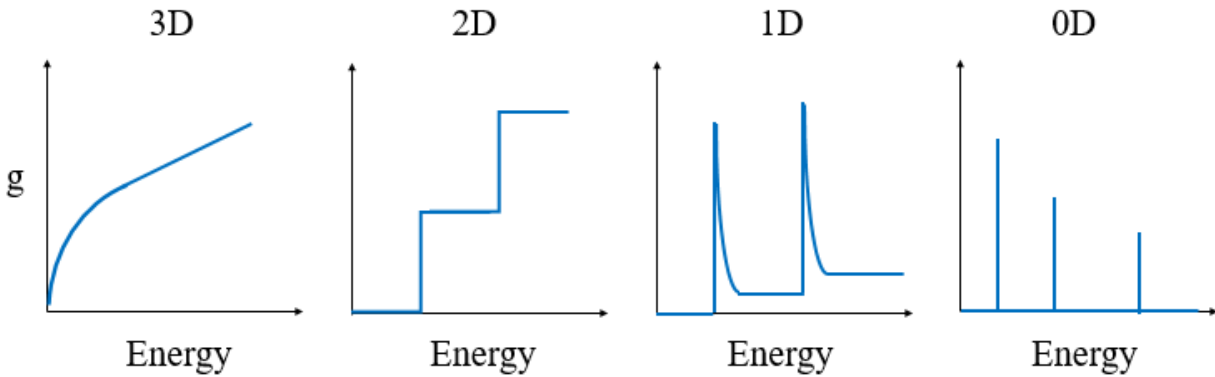


Figure 1.1. The electronic density of states as a function of energy for four different configurations: zero, one, two, and three dimensional.

In bulk material, the valence and conduction bands are continuous. Free electrons and holes are permitted to move about within the conduction and valence band, respectively. When the material is spatially restricted, as in nanostructures, the carriers are confined like a particle in a potential box. Both the bulk energy bands and the discrete energy levels found in nanostructures are illustrated in Figure 1.2. When an electron is excited from the valence band to conduction band, a hole is left behind in the valence band. This electron-hole pair is known as an exciton, which is treated as a quasiparticle. This transition is an interband transition in both bulk and quantum structures. In nanostructures, there are selection rules for which interband transitions are allowed. Transitions are restricted between energy levels of equivalent parity. Intersubband transitions are labeled for the quantum structure and occur within either band. Due to discrete energy levels, the band gap of the material increases as the size of nanostructure decreases.

Quantum confinement occurs when the size of the nanostructure approaches the exciton Bohr radius associated with the material. An exciton is physically modeled after the Bohr model

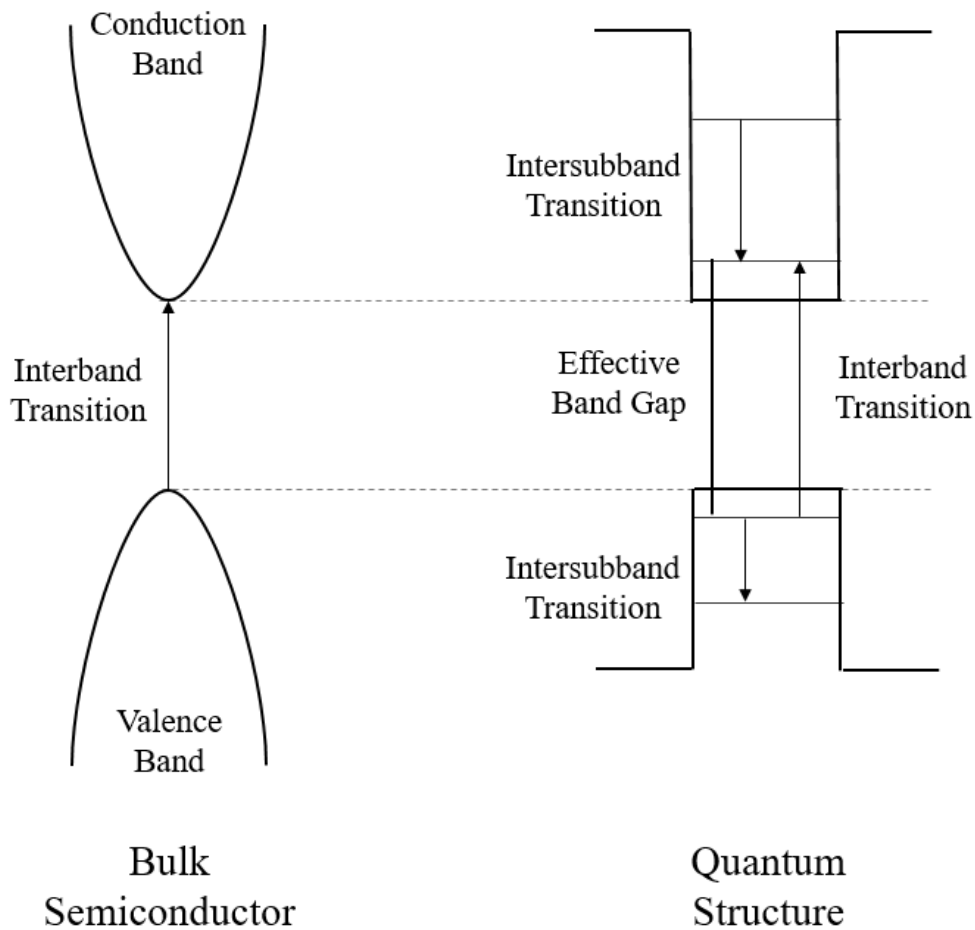


Figure 1.2. The band diagrams of bulk and quantum structures are shown with the interband and intersubband transitions labeled.

of the hydrogen atom, and therefore has analogous properties. At this scale, the charge carriers are spatially confined. The lesser the degree of freedom for a structure, the stronger the quantum confinement effect in the material because the carriers are confined in more dimensions.

Extreme quantum confinement is defined by the condition that the ratio of the radius of the nanocrystal to the exciton Bohr radius of the material is much less than one. The exciton Bohr radius for bulk material can be calculated by using Equation 1.1

$$a_{ex} = \frac{m_0 \varepsilon}{\mu^*} a_H \quad (\text{Equation 1.1})$$

where a_{ex} is the exciton Bohr radius, m_0 is the free electron mass, ε is the dielectric constant, a_H is the Bohr radius of the hydrogen atom (0.5293 Å) and μ^* is the reduced effective mass of the electron and hole. When the exciton Bohr radius of a material is large, the extreme quantum confinement regime can be reached with larger nanoparticles.

At this scale, the energy levels become discrete rather than continuous. Therefore, the band gap is directly dependent on the size of the nanostructure. This allows the band gap to be tuned for specific applications through size adjustments in the synthesis process. The effective band gap is proportional to one over the square of the diameter of the nanostructure, as expressed in Equation 1.2,

$$E_G^* = E_G + \left(\frac{\pi^2 \hbar^2}{2\mu^* d^2} \right) \quad (\text{Equation 1.2})$$

where E_G^* is the effective band gap, E_G is the bulk band gap, \hbar is Planck's constant, μ^* is the reduced effective mass and d is the diameter of the nanocrystal. The reduced effective mass is a combination of the electron effective mass, m_e^* , and hole effective mass, m_h^* , as shown in Equation 1.3.

$$\frac{1}{\mu^*} = \frac{1}{m_e^*} + \frac{1}{m_h^*} \quad (\text{Equation 1.3})$$

Quantum dot composition and the corresponding band structure are shown in Figure 1.3 [27]. A simple core structure exhibits a level band composition. The quasi-type-II core/shell configuration contains a step in the energy bands due to the difference in the energy bands of the core and shell materials. Also, the band alignment indicates that the valence band maximum for the shell material is greater than that of the core. A core/alloyed shell, or quasi-type-II structure, has a smoothed step due to the smooth transition between the core and shell. The gradual change

of the lattice constant reduces the effects of lattice mismatch. The band gap is easily tuned through size adjustments of the nanocrystals. As the width of the well decreases, the effective band gap increases. This allows a material to be functional within a spectral range, from near IR to VIS. The corresponding band structure and electron and hole wave functions are also sketched in the Figure 1.3.

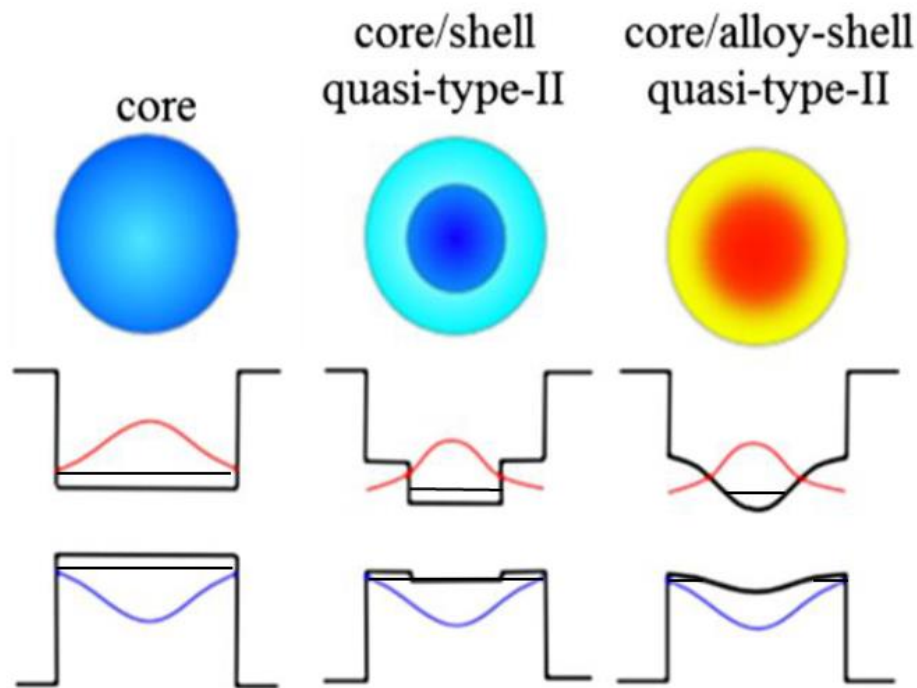


Figure 1.3. A schematic shows how the composition of the nanocrystals changes the band structure of the material [27].

The effective band gap of quantum structures is directly affected by the dimensions of the material. This dependence enables a device to operate within a wide spectral range, from ultraviolet to infrared. Consequently, nanocrystals are suitable for a wide variety of applications, such as photothermal therapy [28], light emitting diodes [9], solar cells [29], and photodetectors

[30]. Nanostructures enable devices to operate in the technologically important infrared region of the spectrum. Infrared light is widely used in applications, such as biomedical imaging and therapy [31][32], solar power harvesting [33], and optical communications [34].

There are a variety of methods to grow nanomaterials. Chemical vapor deposition (CVD) and metal-organic chemical vapor deposition (MOCVD) are widely used to grow very thin films. The instrumentation enables the deposition of one atomic layer at a time, which allows for higher precision. Molecular Beam Epitaxy (MBE) is a commonly used growth method because of its versatility. High quality nanostructures of two, one, and zero dimensions can be formed by MBE. However, the instrumentation necessary is quite expensive and slow deposition rates must be used. Solution-based synthesis procedures can be performed at a much lower cost. Colloidal growth of nanocrystals is a common practice because of the reduced cost and scalability of the procedure. This wet chemical method of growth has repeatedly yielded uniform size distributions. The optical properties of the nanocrystals depend on the size, which can be easily tuned in solution based growth methods, to operate in a desired spectral range for a specific application. Their size is tuned through altering the injection temperature and/or growth time. With a solution-based synthesis process, nanocrystals can be as small as a few nanometers in diameter, which is necessary to reach the extreme quantum confinement regime. For these reasons, a colloidal synthesis procedure was selected for this project.

1.2.2 Pb Compounds

Lead chalcogenides have unique properties, specifically PbS and PbSe. These semiconductors have a rock salt crystal structure, as seen in Figure 1.4, and a direct band gap at

the L-point. Lead salt compounds exhibit a large exciton Bohr radius, which makes reaching the extreme quantum confinement regime possible [35]. These materials are also characterized by a large dielectric constant [36] and a small electron and hole effective mass [37]. The absorbance spectrum ranges from the near infrared to visible range. This allows the material to operate in the technologically important infrared region. Optical communication [34], photovoltaic devices, [4] and some biomedical imaging and therapies [31], [32] operate in the infrared regime. These materials are also fit for use in thermoelectric devices to harvest waste heat.

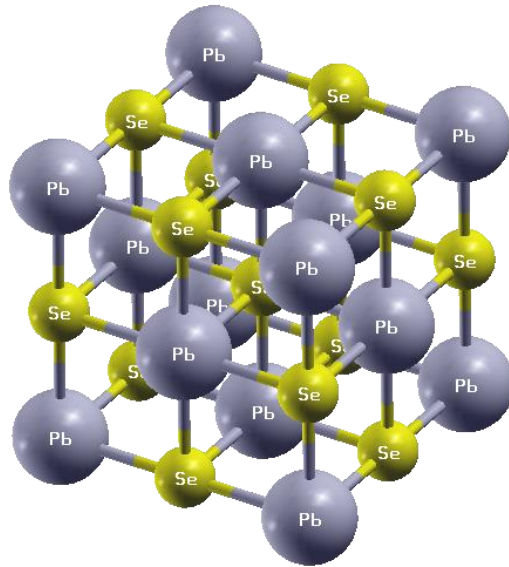


Figure 1.4. The crystal structure of PbSe is zinc blende.

The large exciton Bohr radius associated with these lead salt compounds, especially of PbSe and PbTe as can be seen in Table 1.1, enables access to the extreme quantum confinement regime. This regime is defined by the condition that the ratio of the radius of the nanocrystal to

Table 1.1. The band gap (at room temperature) in eV, exciton Bohr radius in nm, and the effective mass for holes and electrons are listed for the three main lead salt compounds [17].

	Band Gap T = 300K (eV)	Exciton Bohr Radius (nm)	Effective Mass of Hole	Effective Mass of Electron
PbS	0.420	20	0.075 m_0	0.080 m_0
PbSe	0.278	46	0.068 m_0	0.040 m_0
PbTe	0.311	46	0.022 m_0	0.024 m_0

the exciton Bohr radius of the material is much less than one. Ratios down to 0.04 were reported utilizing lead salt compounds, while CdSe quantum dot studies have reached 0.16 [35]. The band gaps at room temperature and effective masses of the electron and hole are also included in Table 1.1. The band diagram for PbSe and PbS is illustrated in Figure 1.5. The band alignment of the core and shell materials, PbSe and PbS, result in a type II configuration. However, since the valence band maximums are so proximate, the carrier wave functions extend from the core into the shell material for sufficiently small nanocrystals (< 10 nm) [38].

A recurring problem with lead selenide nanomaterials is surface instability [39], [40]. The nanocrystals quickly oxidize in atmosphere and this greatly increases the conductivity of the material making it inappropriate for the proposed applications. Oxidation of the surface of lead chalcogenide nanomaterials results in a blue shift in the absorbance and emission spectra. This is due to the fact that the effective core of the nanocrystals shrinks as the surface oxidizes, which increases the quantum confinement [39]. Passivation of the surface is necessary to avoid excessive oxidation. One way to mitigate this negative effect is to grow a protective shell around the core material. This is why the PbSe/PbS core/shell configuration is of special interest. Selenium is a better reducing agent when compared to sulfur, meaning that PbS is more resistant to oxidation than PbSe [41]. A ligand exchange can also passivate the surface of the

nanomaterials. The ligand present in the core at synthesis is oelic acid. This organic ligand can be exchanged for a shorter inorganic ligand that moderately increases the conductivity of the material, making it suitable for electronic applications.

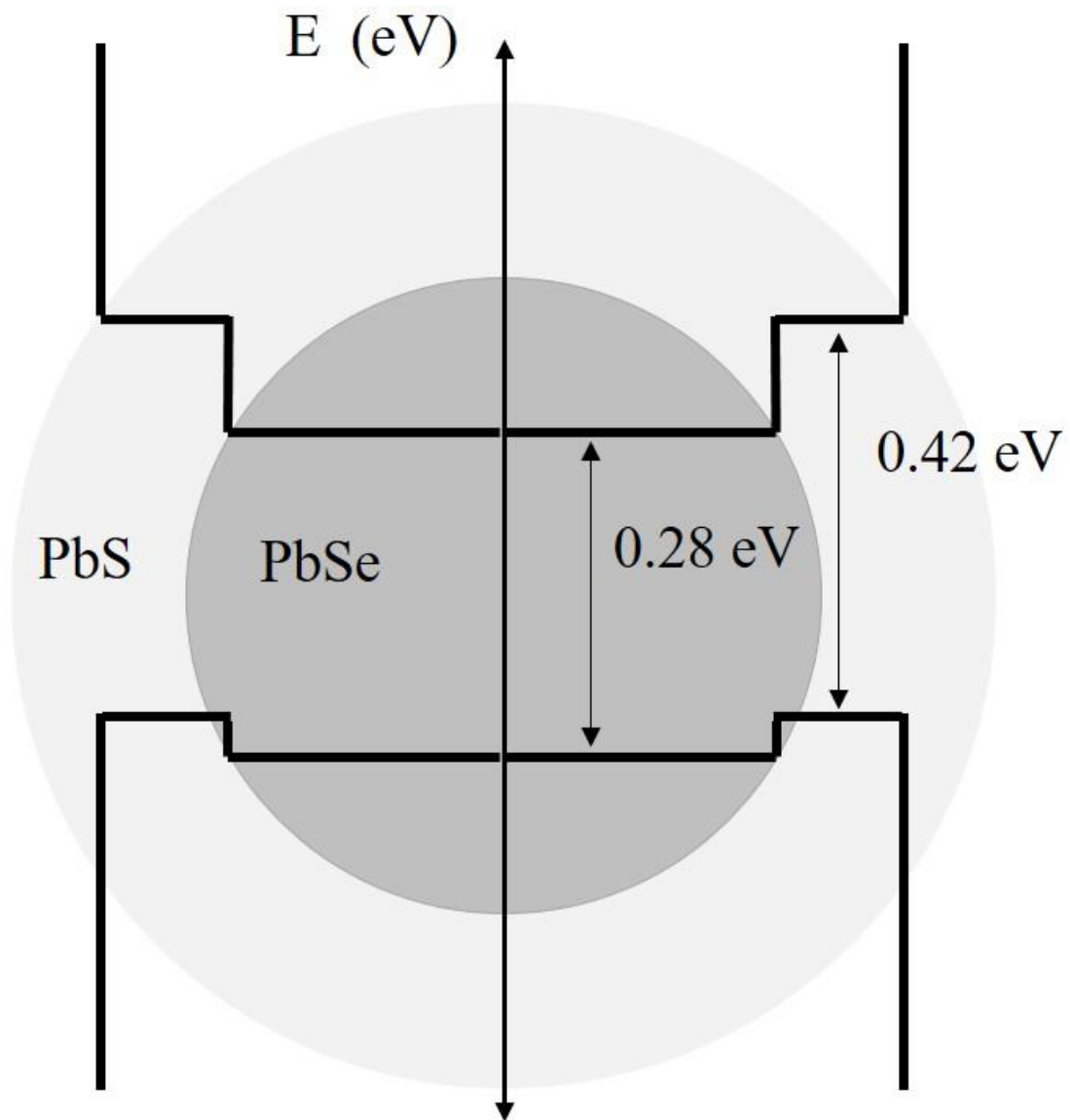


Figure 1.5. The band diagram for PbSe and PbS is shown with energy in eV.

Chapter 2 Experimental Methods

The wet chemical synthesis procedures used in this work are outlined in this chapter. Characterization of these materials include absorbance, photoluminescence, and TEM spectroscopy. The simulation techniques utilized are discussed as well.

2.1 Colloidal Synthesis

The synthesis procedures are detailed in this section for both the core and core/shell structures. Both compounds were grown by a wet chemical synthesis method on an identical setup shown in Figure 2.1. A core/alloy shell configuration was attempted and the synthesis procedure followed is outlined in this section. The major components of the setup are labeled by red letters in the figure. Point A labels the incoming nitrogen flow which flows through the three-neck flask where the chemical reaction took place. Label B represents the temperature probe which sat inside a thermocouple well containing ODE in order to read an accurate temperature of the solution. Label C indicates the stirring apparatus, which operated through an electromagnetic field interacting with a magnetic stirrer bar. The heat mantle is labeled as D and was controlled by the temperature controller labeled as E.

Colloidal synthesis was utilized for the growth of both the PbSe and PbSe/PbS nanocrystals. Generally, a metal precursor is prepared by dissolving the metal in an organic solvent. The solution is then heated and stirred in a flask under an inert gas to a desired temperature. A second solution containing the remaining reagents is then injected into the metal precursor. The quantum dots are then formed through nucleation. The temperature at which

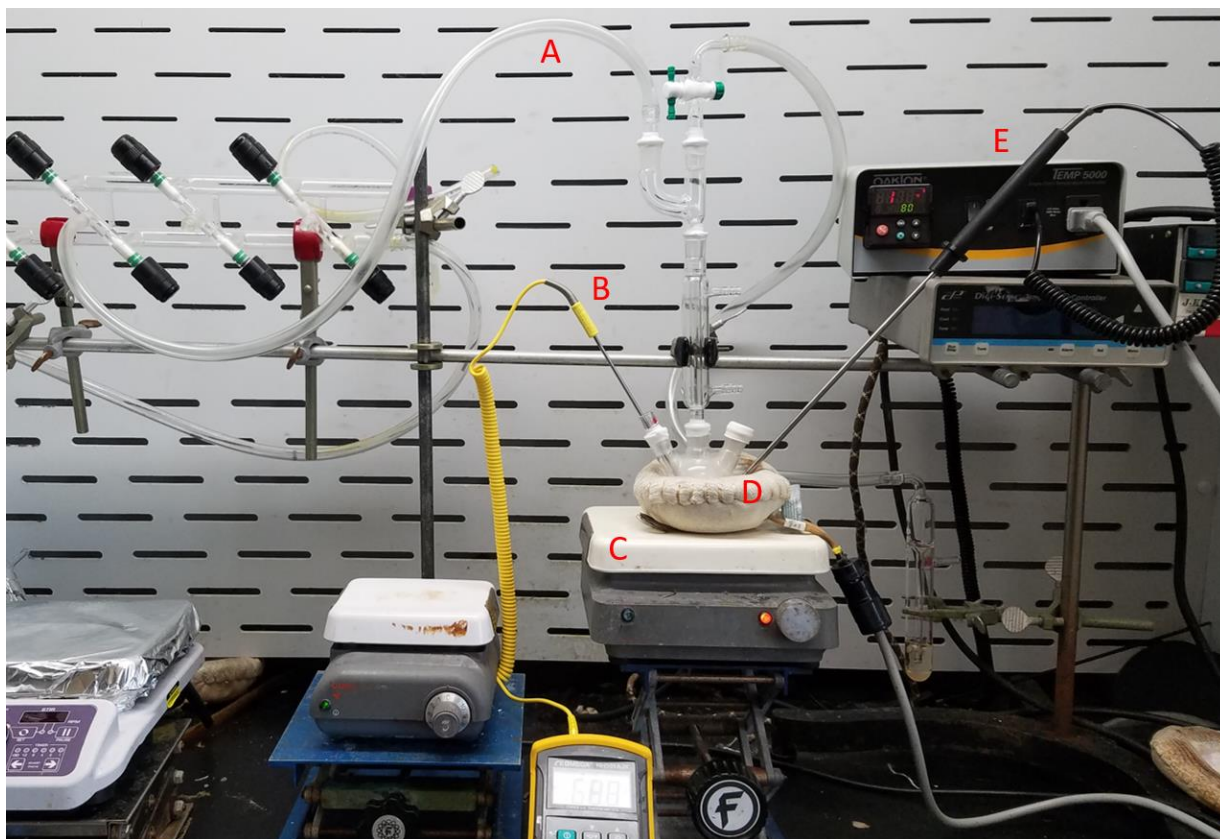


Figure 2.1. The picture of the set up used for all synthesis procedures was taken during synthesis on 04/28/2016 by Haley Morris.

injection occurs and the duration of growth determine the size of the nanocrystals. After the desired growth time, the solution is then quenched until it reaches room temperature in order to stop nucleation. Quenching is done by submerging the flask in water until the solution reaches room temperature. The solution is then purified to remove the excess chemicals that remain after the reaction is complete.

Wet chemical synthesis procedures are much more cost effective than vacuum synthesis techniques, such as CVD, MOCVD and MBE. A simple Schlenk line set up, as shown in Figure 2.1, is all the equipment that is required to perform synthesis. All of this equipment is relatively inexpensive when compared to the complex system required for vacuum techniques.

Deposition of colloiddally grown nanocrystals can be done through various methods, such as drop casting, spin coating and dip coating. These techniques are not as precise as the vacuum techniques listed previously, which provide a high level of control by depositing single layers of atoms at a time. Colloidal growth procedures can be easily scaled up to meet high quotas for commercial use.

2.1.1 PbSe Synthesis Procedure

The PbSe nanocrystals were grown via a wet chemical synthesis method based upon previous work [42]. The selenium precursor was produced by dissolving 0.315 g of selenium powder in a solution of 30 μ L of diphenylphosphine and 4 mL of n-trioctylphosphine (TOP). This mixture was heated to 60 $^{\circ}$ C and left to stir overnight. The lead precursor was prepared in a 50 mL three-neck flask. In this flask, 0.3 g of lead oxide was dissolved in 5.3 mL of 1-octadecene and 1.052 mL of oleic acid. The flask was secured on a Schlenk line under nitrogen flow and heated to 140 $^{\circ}$ C. The solution was stirred at this temperature for one hour to ensure a homogeneous solution. The selenium precursor was then injected into the three-neck flask. The solution was left for 20 s to grow the nanocrystals, after which the flask was quenched until it reached room temperature. The nanocrystals were purified four times by adding an excessive amount of acetone and then centrifuged at 6000 rpm for 5 minutes. For example, a 50 mL centrifugation tube contained, on average, 5 mL of the nanocrystal solution, while the remaining 45 mL was filled with acetone. The growth time was varied to investigate the effects on band structure.

2.1.2 PbSe/PbS Synthesis Procedure

The PbSe/PbS core/shell nanocrystals were grown by a hot-injection method similar to prior research [43]. Approximately 200 mg of PbSe core nanocrystals were dispersed in chloroform, mixed with 1.4 mL of TOP and heated to 60 °C in a glove box. This solution was left under nitrogen atmosphere until all of the chloroform had evaporated. The lead acetate precursor was prepared in a three neck flask on a Schlenk line under nitrogen flow. The 0.2 g of lead acetate was dissolved in a mixture of 2 mL of diphenyl ether (PhEt), 1.5 mL of oleic acid and 8 mL of TOP. This solution was heated to 120 °C for an hour and then cooled to 45 °C. The sulfur precursor was prepared by dissolving 0.10 g of sulfur in 0.3 mL of TOP. Once the sulfur was dissolved, the mixture was added to the PbSe core nanocrystal solution. This new reagent solution was mixed with the lead acetate precursor. Another three-neck flask was prepared on a Schlenk line with 10 mL of PhEt. The PhEt was heated to 180 °C under nitrogen flow. The reagent solution was then injected into the PhEt mother solution and left to grow for 15 minutes. According to prior work [43], each 15 minute increment corresponds to one monolayer of shell growth. After the desired growth time elapsed, the solution was quenched until it reached room temperature. The synthesized nanocrystals were purified in an excess of acetone four times.

2.1.3 PbSe/PbSe_xS_{1-x} Synthesis Procedure

The lead selenide / lead selenide sulfide alloy shell nanocrystals were also grown via a wet chemical method. However, for this structure, the core and shell are grown simultaneously to achieve an alloy shell. The procedure was adapted from previous work [43]. There were four

solutions that were prepared separately. Solution one, referred to as the lead acetate precursor, was prepared by dissolving 0.71 g of lead acetate into a mixture of 2 mL of PhEt, 1.5 mL of OA and 8 mL of TOP in a 50 mL three-neck flask. The flask was placed on a Schlenk line and heated to 120 °C under vacuum for an hour. The flask was then cooled to approximately 45 °C and transferred into a nitrogen-filled glovebox. Another three neck flask was placed on the schlenck line under vacuum containing 10 mL of PhEt, solution two, and heated to 120 °C for an hour. After this hour, the vacuum was replaced with nitrogen flow while the solution heated further to 210 °C. While solution two was heating, solutions three and four were prepared in the glovebox. Solution three, the selenium precursor, consisted of 0.15 g of selenium dissolved in 1.4 mL of TOP. Solution four, the sulfur precursor, was prepared by dissolving 0.10 g of sulfur in 0.3 mL of TOP. Once dissolved, the selenium precursor was added to the vial containing the sulfur precursor, which will be referred to as solution five. While in the glovebox, the lead acetate precursor was added to solution five. This mixture was stirred to achieve homogeneity. Once mixed, the solution was drawn into two syringes and both were simultaneously injected into the three-neck flask of PhEt. It was left stirring for 15 minutes on heat to let the nanocrystals form. After which, the solution was quenched to stop the growth process.

2.2 Characterization Techniques

The absorbance spectra of the nanocrystals were measured at room temperature using a Cary 500 UV-Vis-NIR spectrophotometer[44]. The spectrophotometer produces and directs monochromatic light at the sample and then measures the incident and transmitted spectra over the range of 175 to 3300 nm. The nanocrystals were dispersed in a solvent, chloroform or

hexane, and placed inside a quartz cuvette with a path length of 1 cm for measurement. The solution was tested over a range of wavelengths, from 200 nm to 2000 nm.

When light interacts with a material, it is either absorbed, transmitted or reflected. Absorbance is a measure of how much of the incident light is neither transmitted nor reflected. It depends on the composition of the material and how light of different wavelengths interact with the material. Absorbance is quantified in Equation 2.1,

$$A = -\log \left[\frac{I}{I_0} \right] = \log \left[\frac{I_0}{I} \right] \quad (\text{Equation 2.1})$$

where I is the transmitted intensity, I_0 is the incident intensity and A is absorbance [45]. If the light has less energy than the band gap of the material, it is either reflected or transmitted. If the light has sufficient energy, an electron will elevate from the valence band to the conduction band. This is called an interband transition.

The photoluminescence (PL) measurements were made with a Bomem BA8 Fourier Transform spectrometer[46]. The samples measured were formed by dropping the nanocrystals, while dispersed in a solvent, onto a glass slide. This was repeated until a thin layer of nanocrystals was left on the slide after the solvent evaporated. The samples were then placed in the cryostat and the chamber was brought down to vacuum. Liquid nitrogen was used to bring the temperature to approximately 77 K in order to reduce thermal contributions. The PL spectra is reported as intensity versus wavelength.

The PL measurements reveal the emission spectra. Electrons within the material are excited by shining a laser on the sample. The Bomem uses a source of 642 nm. As the electrons drop to lower energy levels, they emit light which is detected by the spectroscopy apparatus. The PL spectra is a measurement of the energy or wavelength of that light. The data is

represented by intensity vs. wavelength. The distribution of the energy detected reveals the band structure of the material. It is also an indication of the size distribution of the nanocrystals.

Transmission electron microscope (TEM) images were captured with a FEI Titan 80-300 S/TEM[47]. The Titan is capable of imaging at a resolution below 0.1 nm with the help of a CEOS spherical aberration corrector. The nanocrystals dispersed in a solvent were dropped onto a small copper grid coated with a carbon film. The samples were left in air until the solvent had completely evaporated, then they were ready for imaging. Images were taken at several different locations on the grid. A fast Fourier transform (FFT) of the TEM images was also performed in a program called ImageJ [48]. ImageJ is an open source, java platform for image analysis provided by the National Institute of Health. The FFT of the image reveals the lattice structure of the sample. Transforms of a single crystallite and multiple crystallites were performed.

Electron diffraction is utilized in the capture of TEM images. Electrons are generated by an internal source and accelerated across an electric field towards the sample in vacuum. Each electron gains a known amount of kinetic energy through this process. The electron beam is refocused with electromagnetic fields before making contact with the sample. The crystalline lattice that the electrons are incident upon acts as a diffraction grating. The incident and reflected electrons are represented as arrows in Figure 2.2. Two different planes with two different interplanar spacings are depicted with dashed lines. The transmitted electrons are recorded and presented as a magnified image of the sample where individual atoms are visible. The application of a FFT to a TEM image transforms the information into reciprocal space. The resultant diffraction pattern is useful in determining the lattice orientation. Each concentric ring in a FFT image of many nanoparticles represents different planes, each with unique interplanar spacing. When a FFT is taken of a single nanocrystal, the individual atoms are visible.

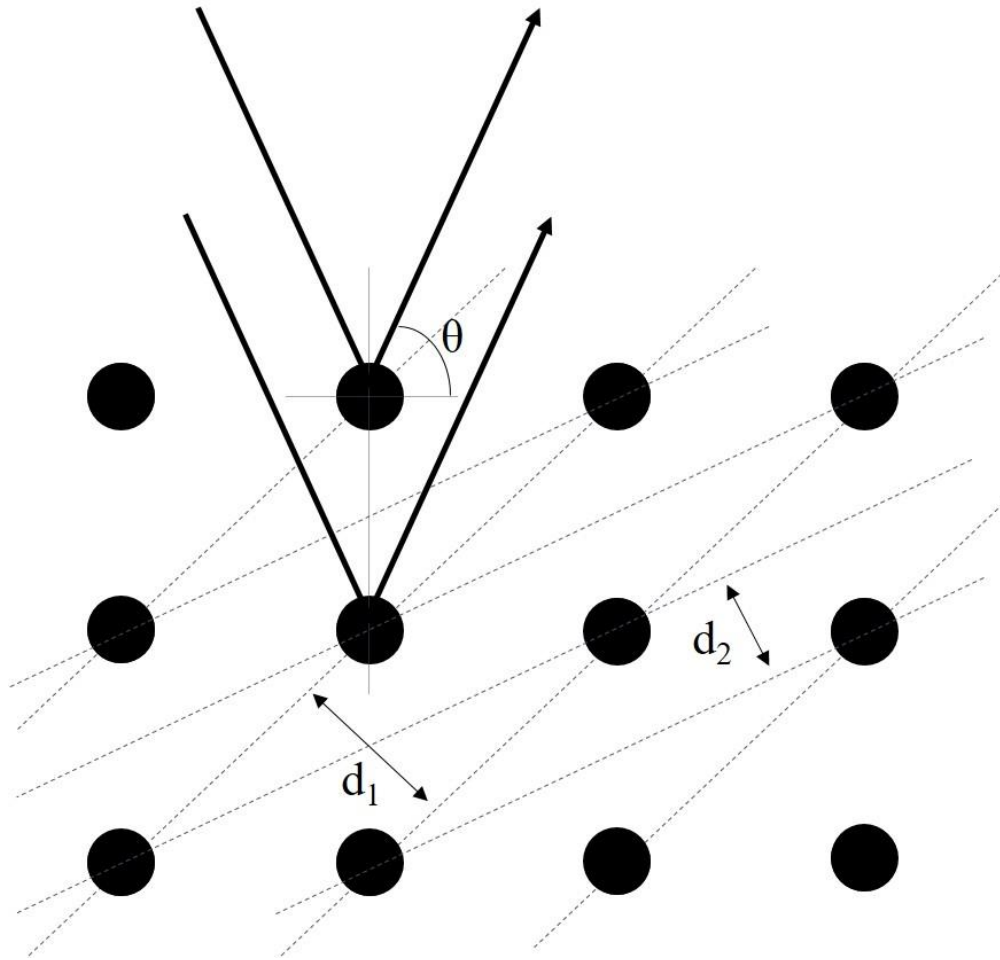


Figure 2.2. A cubic lattice is presented with the dashed lines representing different planes. The differing interplanar distances are labeled for the two orientations depicted.

Furthermore, the Titan is capable of energy-dispersive x-ray spectroscopy (EDX). The EDX measurements yield an elemental analysis of the material tested. This is done by bombardment of high-energy charged particles at the sample. As a result, electrons in the material absorb the energy and are ejected. Electrons will fall back to these vacated energy states resulting in the release of energy in the form of x-rays. This emission spectrum is measured and different elements are identified due to the unique energy levels found in all materials.

2.3 Simulation Techniques

The calculations were executed using the linearized augmented plane wave (LAPW) method as implemented in WIEN2k [49]. This method divides the unit cell between an interstitial region and muffin tin (MT) spheres. This division is depicted in Figure 2.3. The MT spheres are centered at each atom and do not overlap. Within these spheres, there exists a linear combination of radial wavefunctions according to the approximation. The remaining space, the interstitial region, is modeled by plane waves. Functions on the boundary between these two regions are continuous. The LAPW method is a way to solve the equations of density functional theory (DFT) and is an all electron model [50]. This means that all electrons, core and valence, are considered in the calculations. Density functional theory describes a many body problem through functionals of electron density, thereby reducing the computational power necessary to

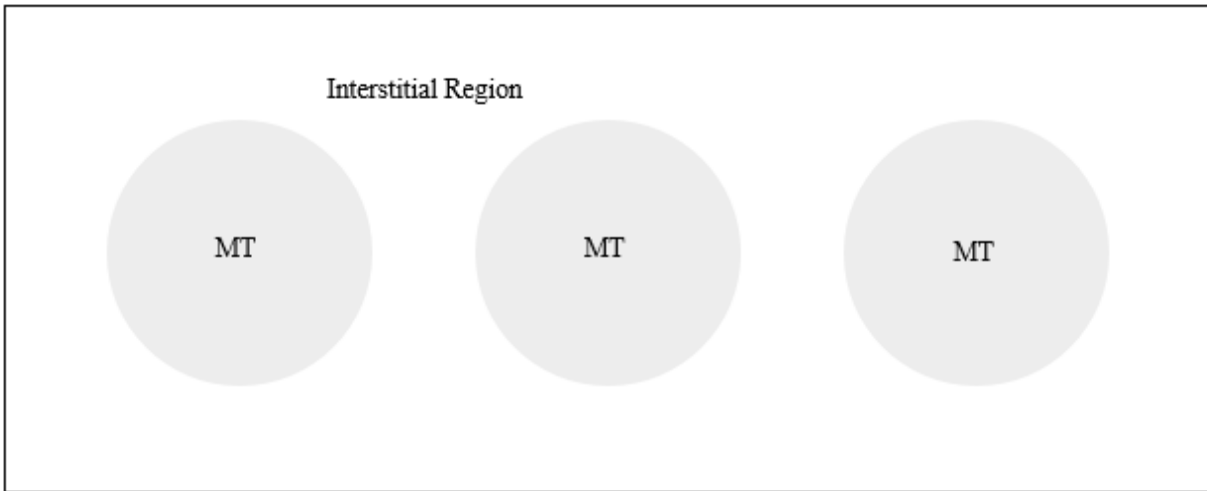


Figure 2.3. The schematic depicts how a material is divided into spherical muffin tins, modeled by linear combinations of radial wavefunctions, and the remaining space is the interstitial region which is modeled by plane waves.

simulate materials. The electron density is determined through self-consistent calculations in which the density is repeatedly changed until it converges. Many computational scientists in physics, material science, and chemistry utilize DFT to model electronic structures [51]. The LAPW method was implemented within the local density approximation (LDA).

When constructing a material in WIEN2k, the elements and space group of the material had to be designated. Then, a k-mesh was chosen depending on the complexity of the material. The larger the k value, the denser the mesh and more intensive the calculations. The lattice constant had to be optimized. An experimental value for the lattice constant was entered. This value, along with incrementally larger and smaller percentages of the experimental value, were used to run the calculations. The resultant total energies were plotted as a function of these lattice constants. The parameter corresponding to the minimum energy was used for all further calculations.

Chapter 3 Results and Discussion

The core material studied, PbSe, was simulated using WIEN2k to better understand the electronic structure. Bulk PbSe was simulated and analyzed in WIEN2k. The crystal structure, band structure, electron density, and density of states are presented and discussed. The PbSe and PbSe/PbS nanocrystals were successfully synthesized and characterized. Absorbance, photoluminescence, and TEM images are presented and discussed in the following subsections. An alloy shell, PbSe/PbSe_xS_{1-x} core/alloyed shell, was attempted. However, synthesis was unsuccessful.

3.1 Simulation Results

Lead selenide has a rock salt structure, shown at two different angles in Figure 3.1. The grey atoms represent lead, and the yellow atoms represent selenium. The cubic rock salt

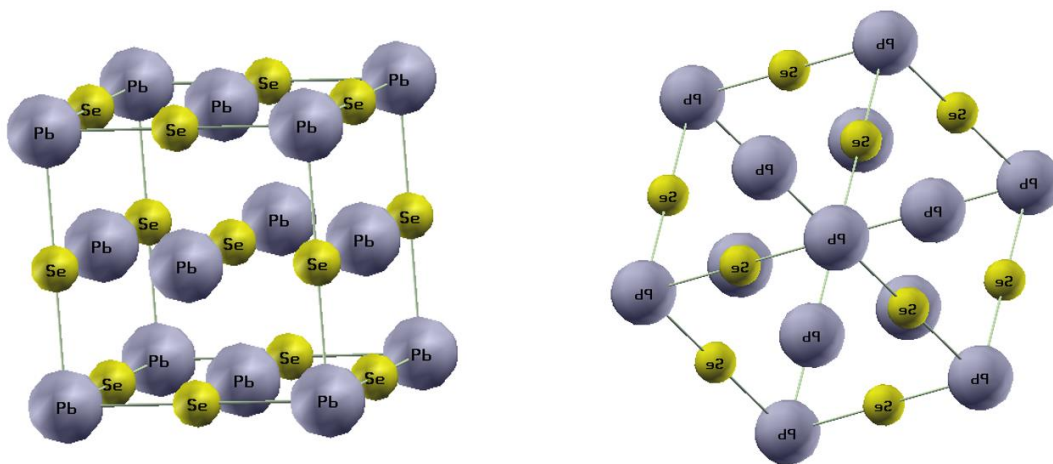


Figure 3.1. The crystal structure of PbSe is rock salt. Two different angles of the material are shown and were generated using WIEN2k and XCrysDen.

structure belongs to the space group $Fm\bar{3}m$, or No. 225 [37]. This crystal structure is equivalent to two offset face centered cubic lattices, one of lead and one of selenium. The unit cell was repeated in three dimensions to approximate bulk PbSe. The electronic calculations were made for this periodic structure in WIEN2k.

A cubic unit cell of PbSe was modeled with a lattice constant of 6.22 Å. This constant was chosen carefully because of its substantial effect on the band gap. The lattice parameter was selected through structural optimization. The total energy of the unit cell was calculated for an experimentally determined lattice constant of 6.11 Å and for $\pm 15\%$, $\pm 10\%$ and $\pm 5\%$ of this experimental constant [23]. The volume optimization curve was plotted and approximates a parabola, as is shown in Figure 3.2. The lattice constant corresponding to the minimum total

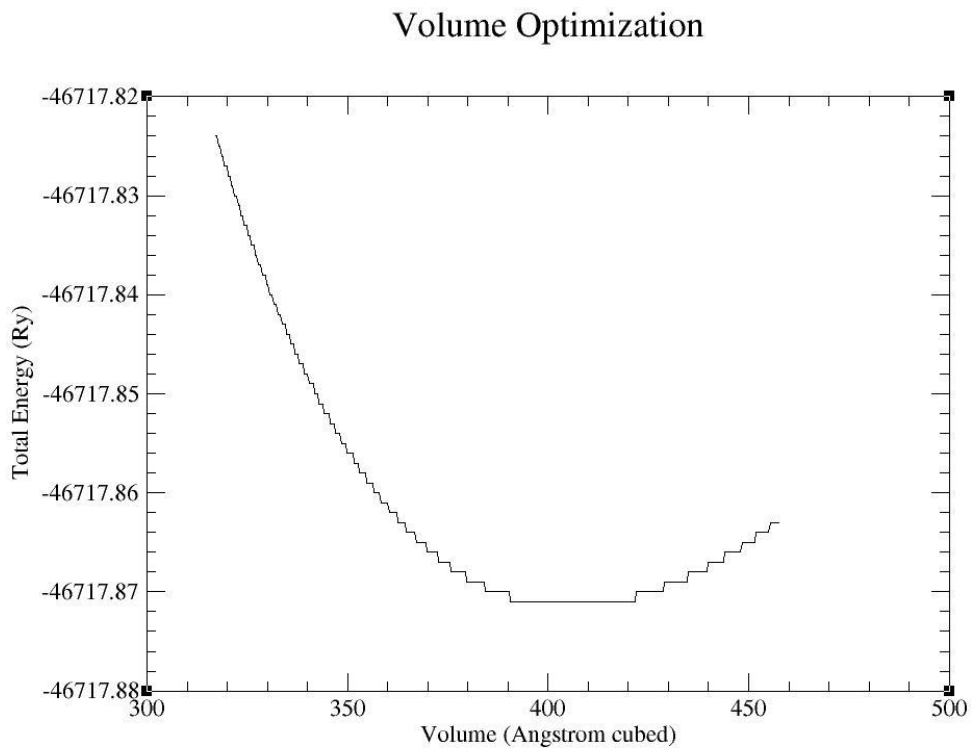


Figure 3.2. The volume optimization curve is plotted as total energy in Rydberg vs. volume in cubic angstroms.

energy was selected for all further calculations, which was 6.22 Å. Previous research conducted by Wei and Zunger computing electronic and structural characteristics of lead chalcogenides using the LDA calculated a lattice constant of 6.098 Å for PbSe [52]. Another study evaluated PbSe using the LDA and generalized gradient approximation (GGA) and calculated lattice constants of 6.053 Å and 6.196 Å, respectively [53]. The calculated lattice constant of 6.22 Å is in good agreement with the GGA calculation, 0.39% (percent difference), and LDA calculation, 2.72%. The lattice parameter of 6.22 Å is in fair agreement with Wei and Zunger with only a 2% difference. The calculated lattice constant is 1.8% percent greater than the experimental lattice constant of 6.11 Å. In a similar computational study, Ekuma et al. used a lattice constant of 6.124 Å, a 1.56% difference [54].

The electronic band structure was calculated for bulk PbSe. The results are shown in Figure 3.3, which indicates a direct band gap at the L point in the Brillouin zone. This characteristic is consistent with the literature [52]–[56]. The difference between the valence band maximum (VBM) and conduction band minimum (CBM), both of which are located at the L point, is the band gap, which is 0.40 eV. Similar studies have yielded values between 0.38 eV and 0.17 eV [52]–[54]. The band gap calculated is at least 5% larger than any simulated values found in the literature review.

The electron density, $n(r)$, was calculated for the PbSe structure. This density reflects the probability of an electron occupying a point in space. Density functional theory is a way to analyze a material in the framework of functions of electron density functions. This approach reduces the computational power required to model compounds. The electron density for bulk PbSe, as calculated, is presented in Figure 3.4. Electron density is denoted as $n(r)$, since it is

dependent upon the distance from the center of each atom, r . The legend indicates the scale represented by increments, $\Delta n(r)$.

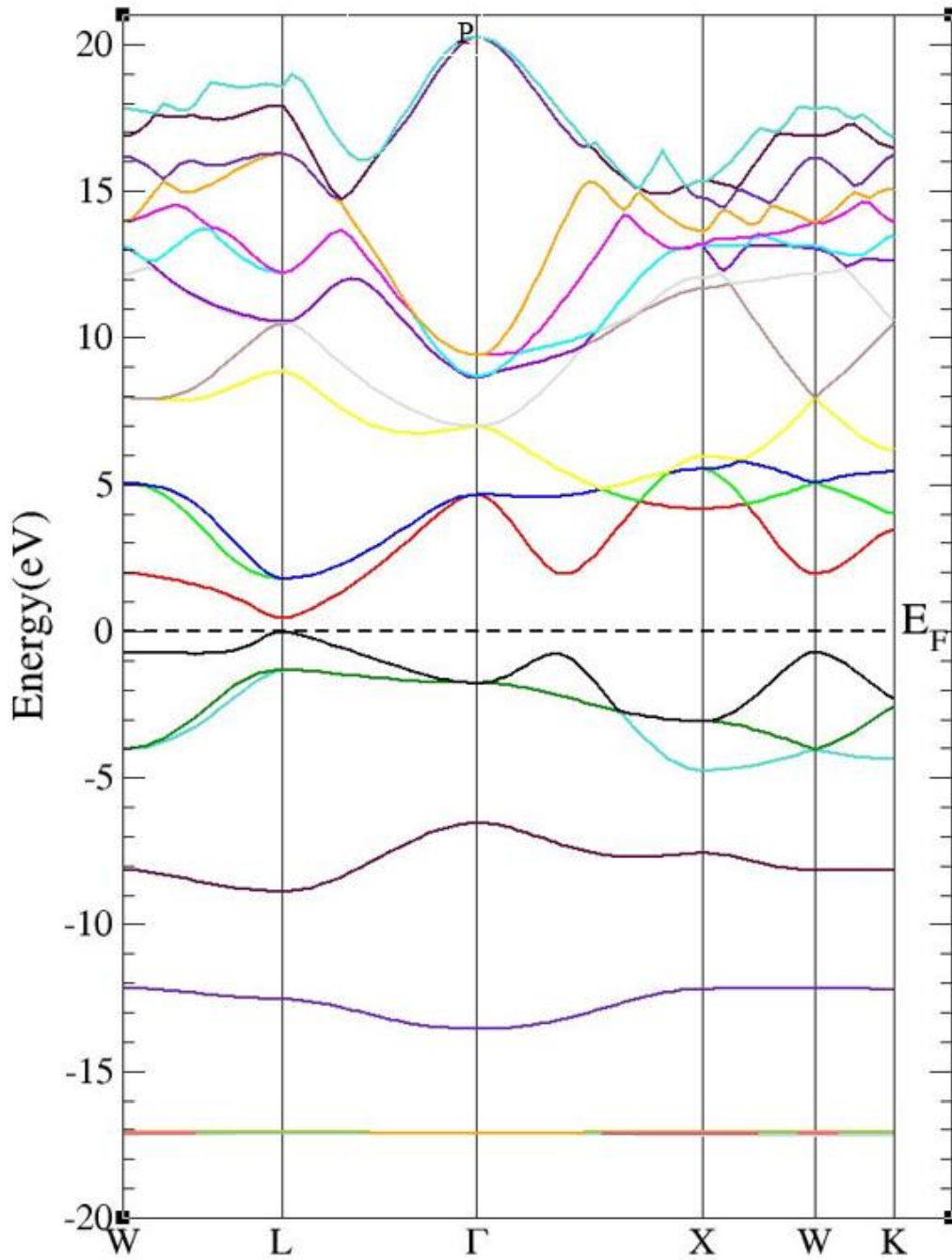


Figure 3.3. The full band diagram for bulk PbSe shows the direct band gap of 0.40 eV found at the L point.

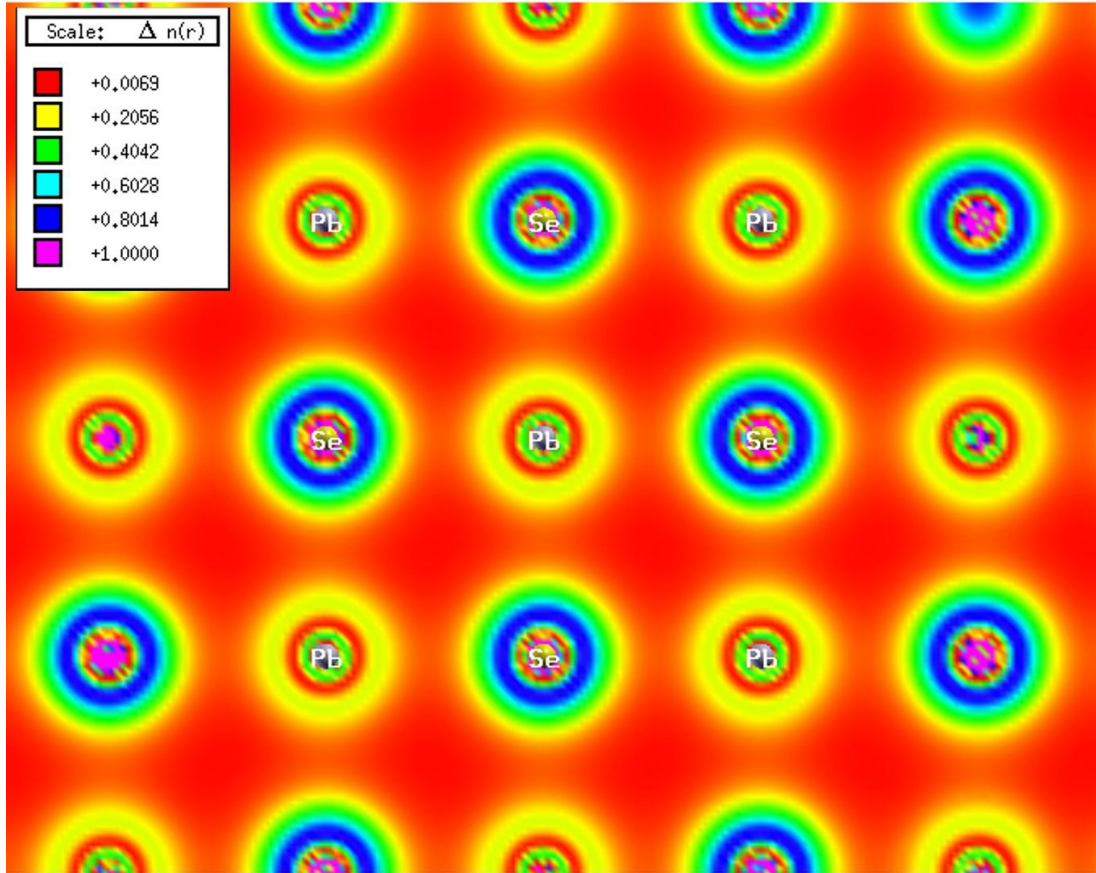
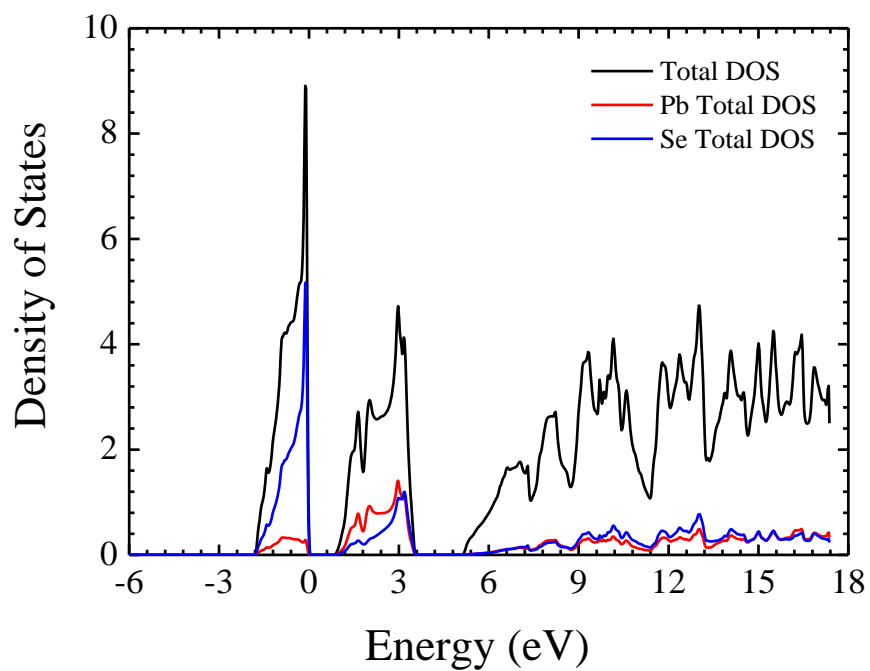
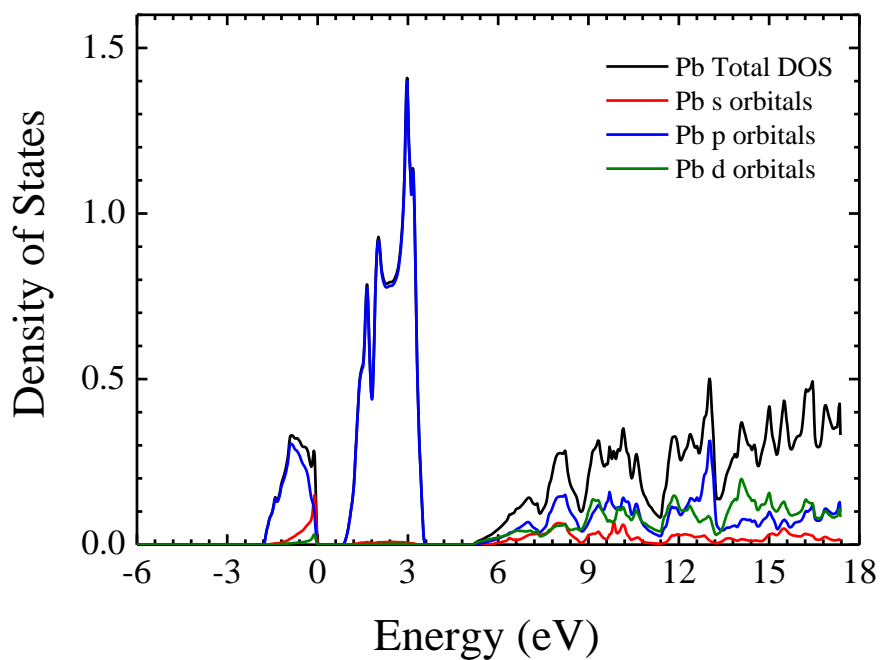


Figure 3.4. The electron density was calculated in WIEN2k. The lead and selenium atoms are labeled.

The density of states (DOS) is the energy distribution of states in a material. This was calculated for bulk PbSe and the total and separate contributions of the lead and selenium atoms were plotted for comparison in Figure 3.5 (a). The selenium contribution, in blue, dominates the total DOS. The lead contribution is shown in red. The DOS for lead and selenium was calculated by orbital levels, as shown in Figure 3.5 (b) and (c), respectively. For lead and selenium, the p orbital dominates the DOS, except at high energies (greater than 13 eV for Pb and 7 eV for Se) where the d orbital has a higher density of states. The s orbital is the lowest contributor for both lead and selenium.

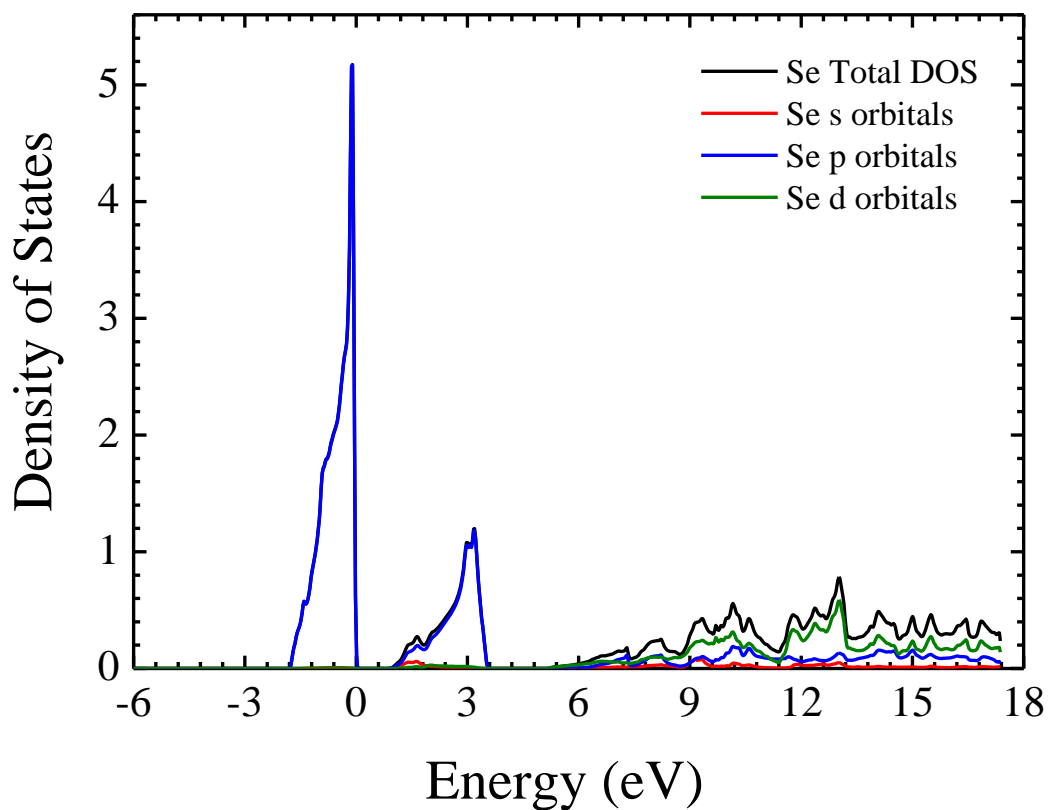


(a)



(b)

Figure 3.5. The contributions to the density of states of PbSe were calculated and plotted as a function of energy. (a) The total density of states for PbSe as well as the lead and selenium contributions. (b) The Pb contribution to the density of states and its orbital contributions: s, p and d.



(c)

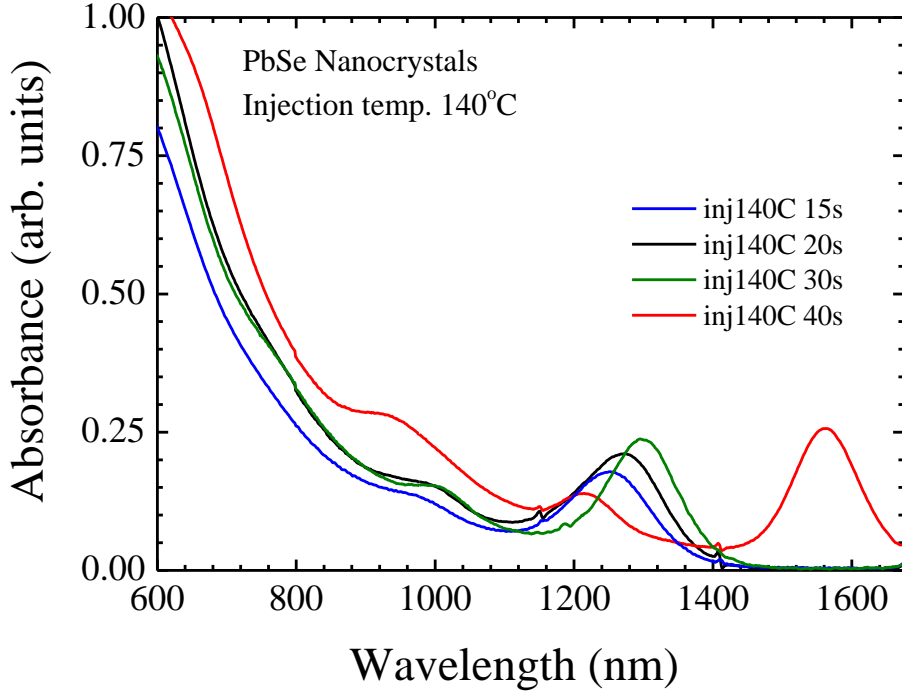
Figure 3.5., cont'd. (c) The Se contribution to the density of states was divided between the s, p and d orbitals.

3.2 Experimental Results

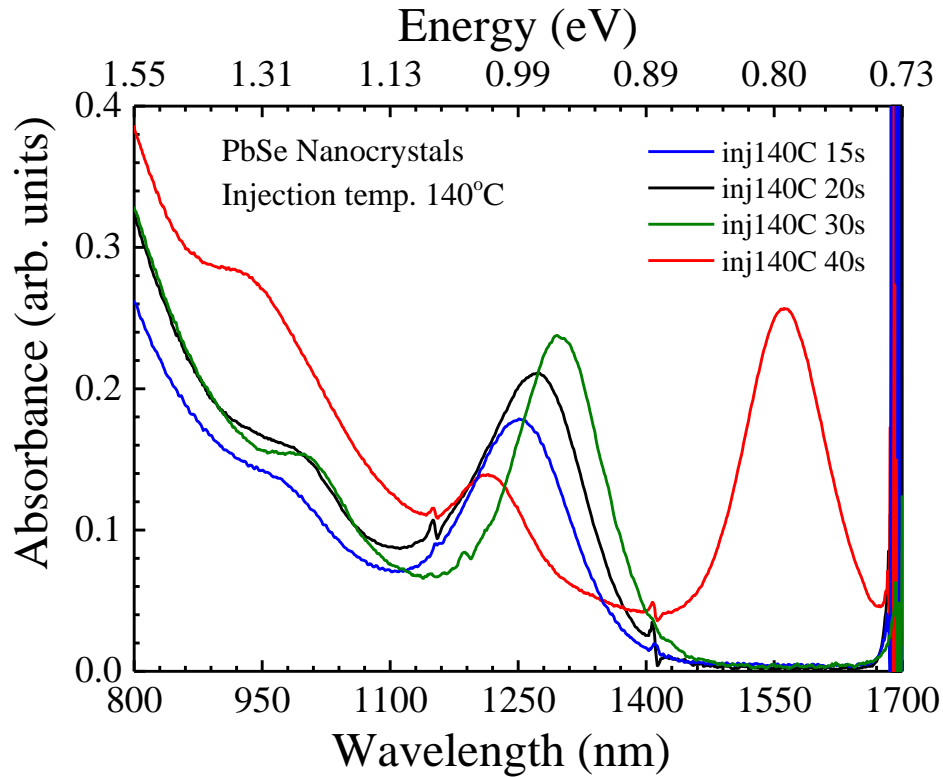
The experimental results for PbSe, PbSe/PbS and PbSe/PbSe_xS_{1-x} are presented and discussed in this section. Absorbance, photoluminescence, and TEM measurements for the PbSe and PbSe/PbS nanocrystals are presented and discussed in the following subsections. The alloy shell synthesis was unsuccessful, and is discussed in Section 3.2.3.

3.2.1 PbSe

The PbSe colloidal nanocrystals were characterized through absorbance, photoluminescence and TEM measurements. The room temperature absorbance spectra for PbSe core nanocrystals with four different growth times (all injected at 140 °C) are shown in Figure 3.6 (a). A longer growth time allowed further nucleation, and led to an increase in nanocrystal diameter. It is well established that as the size of the nanocrystals increases, the band gap decreases [43], [57]–[59] and approaches that of the bulk PbSe, which is 0.27 eV [60]. The significant blue shift from bulk in the absorbance spectra was expected as a result of extreme quantum confinement as observed in the work Du *et al.* [57]. Also, the peaks observed in the spectra illustrate the discrete energy levels found in sufficiently small nanocrystals [61]. All of this behavior was observed in the absorbance spectra. There exists two discontinuities in each absorbance spectrum at approximately 1407 and 1158 nm. These discontinuities are artifacts that result from referencing the chloroform or hexane baseline. At least three distinct peaks are apparent for each sample, termed excitonic peaks. Figure 3.6 (b) contains the same data as graph (a), but the first exciton peaks are magnified for clarity. The first exciton peaks are observed at 1253, 1267, 1300 and 1562 nm for a growth time of 15, 20, 30 and 40 s, respectively. These peaks correspond to the first interband transitions in the PbSe nanostructures, and are the most intense because this transition is associated with the greatest oscillator strength. The energies corresponding to the onset of absorbance for PbSe nanocrystals of 15, 20, 30 and 40 s are 0.899, 0.888, 0.879 and 0.729 eV. These energy band gaps are larger than the bulk band gap of PbSe due to quantum confinement, and are consistent with similar works [43], [59]. Secondary transitions are visible in all of the absorbance spectra in Figure 3.6 (a), and a tertiary transition is



(a)



(b)

Figure 3.6. The absorbance spectra at room temperature of PbSe nanocrystals with four different growth times dispersed in either chloroform or hexane is plotted in (a). An enlarged plot of the first excitonic peak is shown in (b).

visible for the nanocrystals with a growth time of 40 s. These are also excitonic peaks resulting from interband transitions of different energies. The prominence of these more energetic absorbance peaks may indicate a small size distribution of nanocrystals.

The TEM images and FFT images obtained for the PbSe sample grown at 140°C for 20 seconds are shown in Figure 3.7. A TEM image of the nanocrystals is shown in Figure 3.7 (a). The average size of the nanocrystals measured utilizing ImageJ was 3.242 ± 0.3289 nm. An enlarged section of image (a) is presented in Figure 3.7 (b). The interatomic spacing was measured for 10 different pairs of nearest neighboring atoms in ImageJ [48], for an average of 3.34 Å. Twice the interatomic spacing, which is 6.68 Å, is the lattice constant of the rock salt nanocrystal as measured from the TEM images. The fast Fourier transform (FFT) of the image in (a) is shown in Figure 3.7 (c). Performing a FFT on an image of particles transforms that information into reciprocal space. Concentric rings are visible, each indicating a different interplanar spacing corresponding to a different plane found in a lattice [62]. The diameter of the two center rings were measured in ImageJ. The primary and secondary rings have an average diameter of 4.55 and 6.35 nm⁻¹, respectively. The interplanar distances associated with the primary and secondary rings are 4.40 and 3.15 Å, respectively. The FFT in Figure 3.7 (d) is the transform of (b), a single crystalline nanoparticle. Therefore, there are not concentric rings, but discrete points of light in a cubic structure. The measured interatomic distance in this FFT image is 1.13 nm⁻¹, corresponding to a lattice constant of 5.65 Å.

The gray value of each pixel is presented as a function of distance in nanometers in Figure 3.8. The y-axis is the gray value of each pixel across the PbSe core nanocrystal, as seen in the PbSe TEM inset image. The total distance, 4 nm, was divided by the number of cycles, 12, in order to find the interatomic spacing. A value of 3.33 Å was calculated, which corresponds to

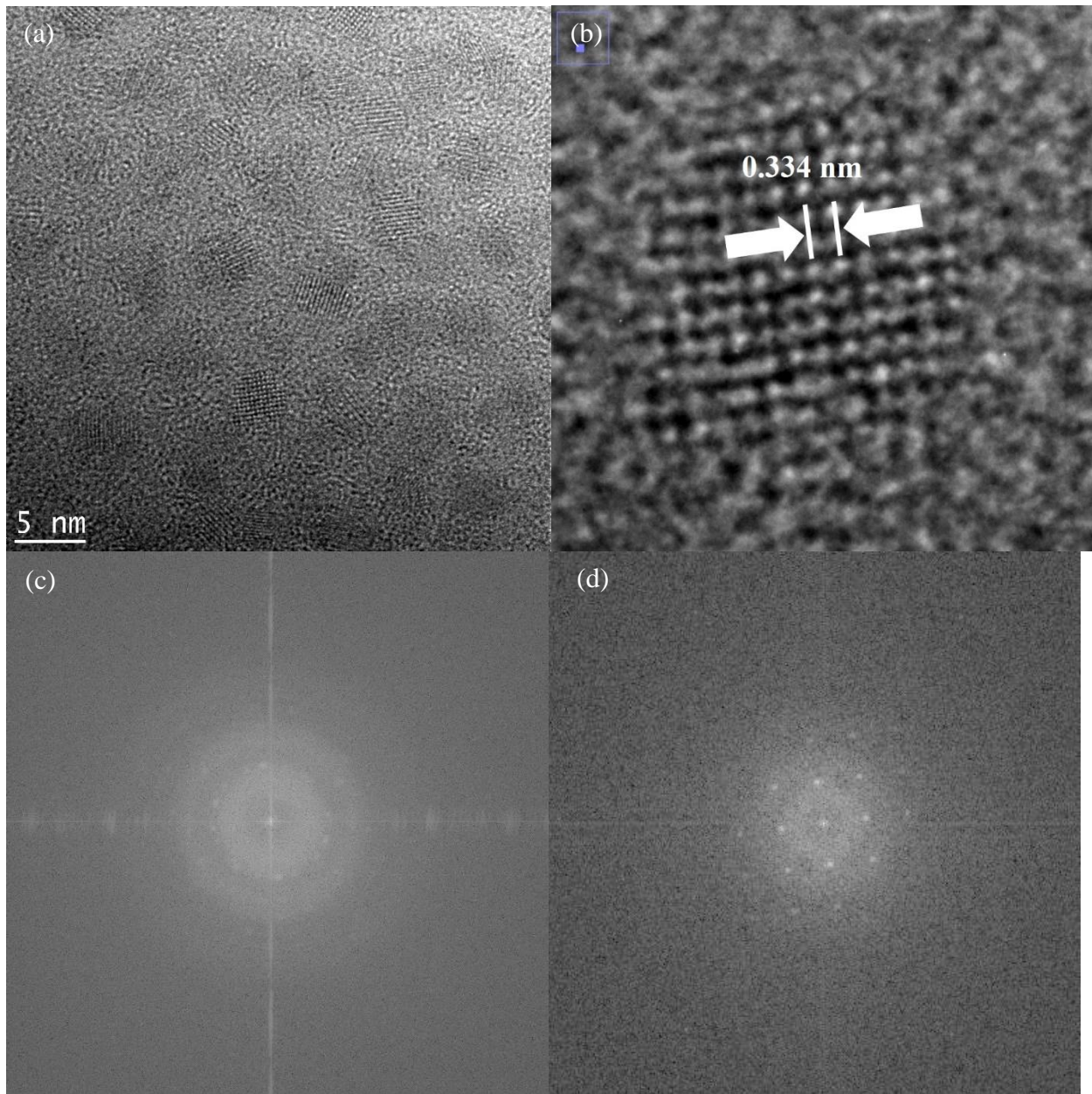


Figure 3.7. Image (a) is a TEM image of the PbSe nanocrystals grown at 140 °C for 20 seconds. Image (b) is a close up of image (a) with the average measured interatomic distance of 3.34 Å labeled. Image (c) is a FFT of image (a) consisting of multiple nanocrystals. In image (d), a FFT was performed in ImageJ on image (b), a single nanocrystal.

A lattice constant of 6.66 Å for the rock salt crystals structure. The three methods used to calculate the lattice constant are in good agreement, except for the FFT method which is approximately 16% different.

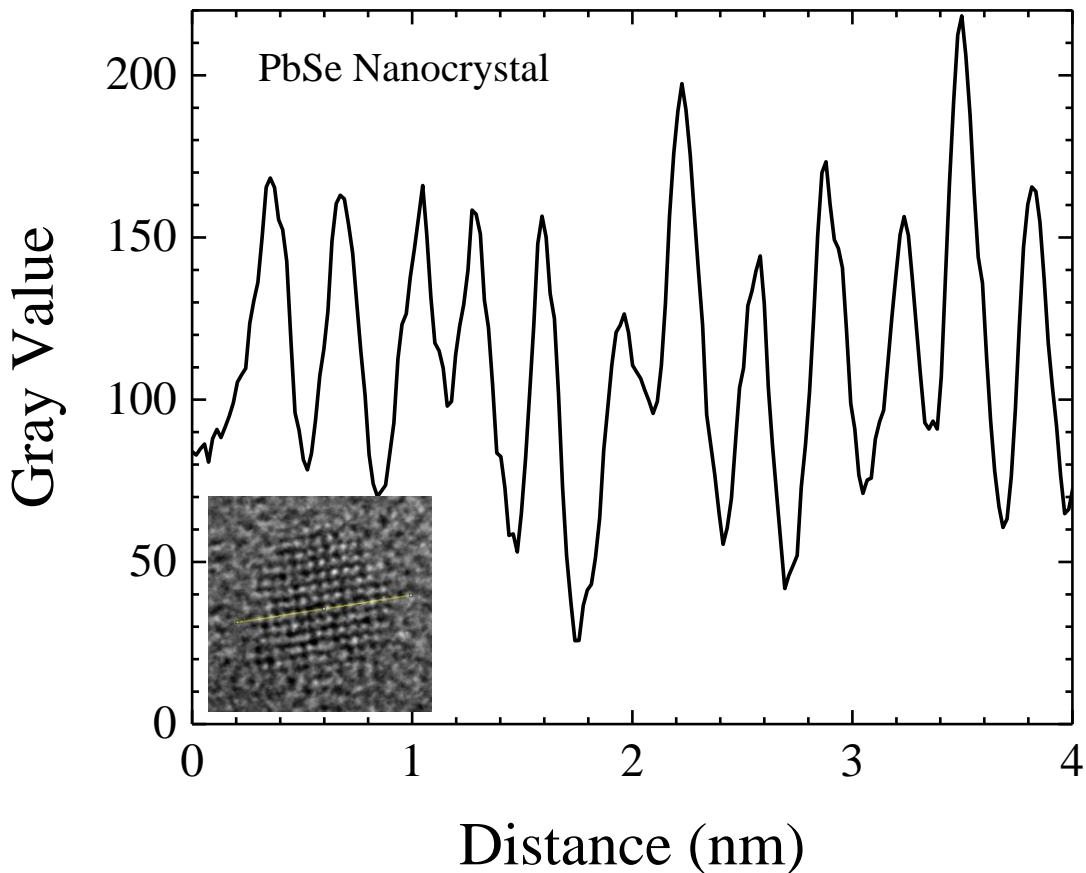


Figure 3.8. The gray value of each pixel along a bisecting line of the nanocrystal is presented as a function of distance in nanometers. The PbSe TEM inset displays the cross-section measured as a yellow line. The interatomic spacing is 3.33 Å.

The TEM is capable of energy-dispersive x-ray spectroscopy (EDX) measurements. The results are shown in Figure 3.9. Lead and selenium are the two most prominent elements. However, carbon, copper and oxygen are also present. The sample was imaged on a copper grid with a carbon coating, and was exposed to air before measurement.

The absorbance and PL spectra for PbSe nanocrystals grown for 20 s are shown in Figure 3.10 and were measured at 300 K and 77 K, respectively. The absorbance spectrum contains the

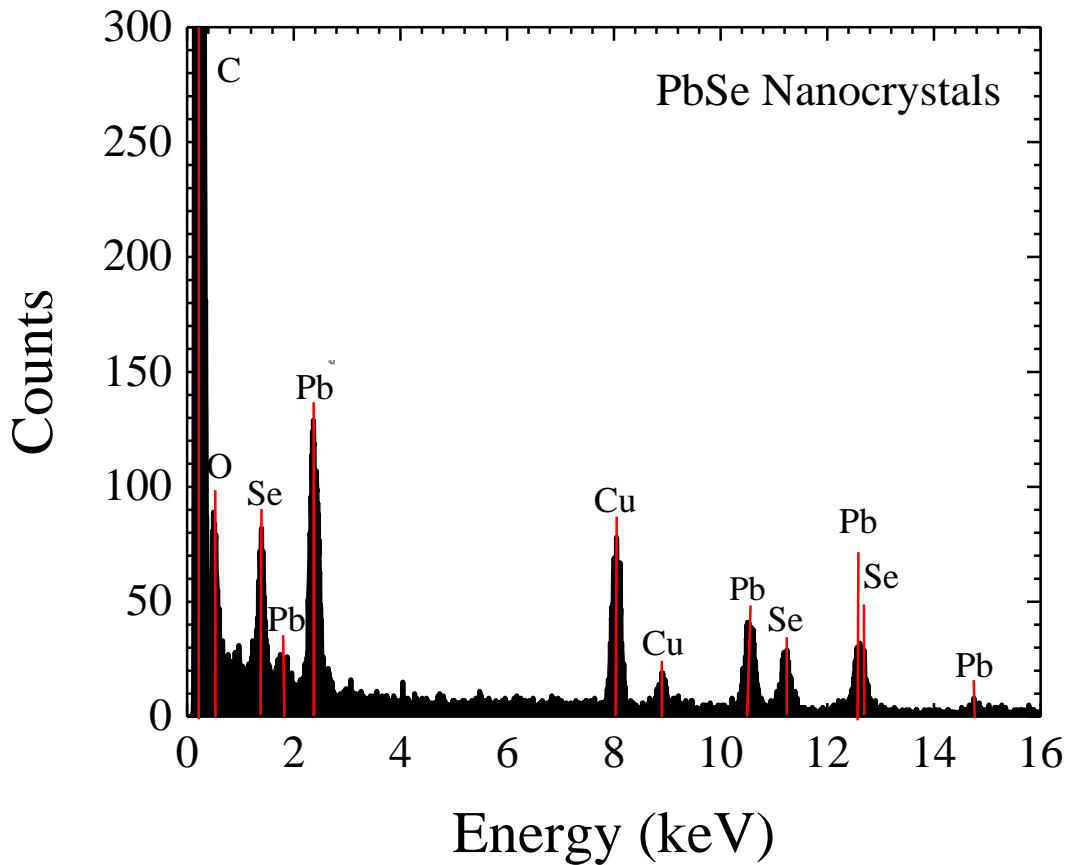


Figure 3.9. Energy-dispersive X-ray spectroscopy results for PbSe nanocrystals.

same two discontinuities as discussed above. The first and second exciton peaks of the absorbance spectra are located at a wavelength of 1315 and 1019 nm, respectively. The first exciton peak energy of the absorbance spectrum is in agreement with the linear trend with respect to the size of nanocrystals given in Brumer *et al.* [43]. However, the peak energy of the PL spectrum is smaller and differs by approximately 50 meV. This difference could be attributed to the fact that the PL measured in Brumer *et al.* [43] was at room temperature

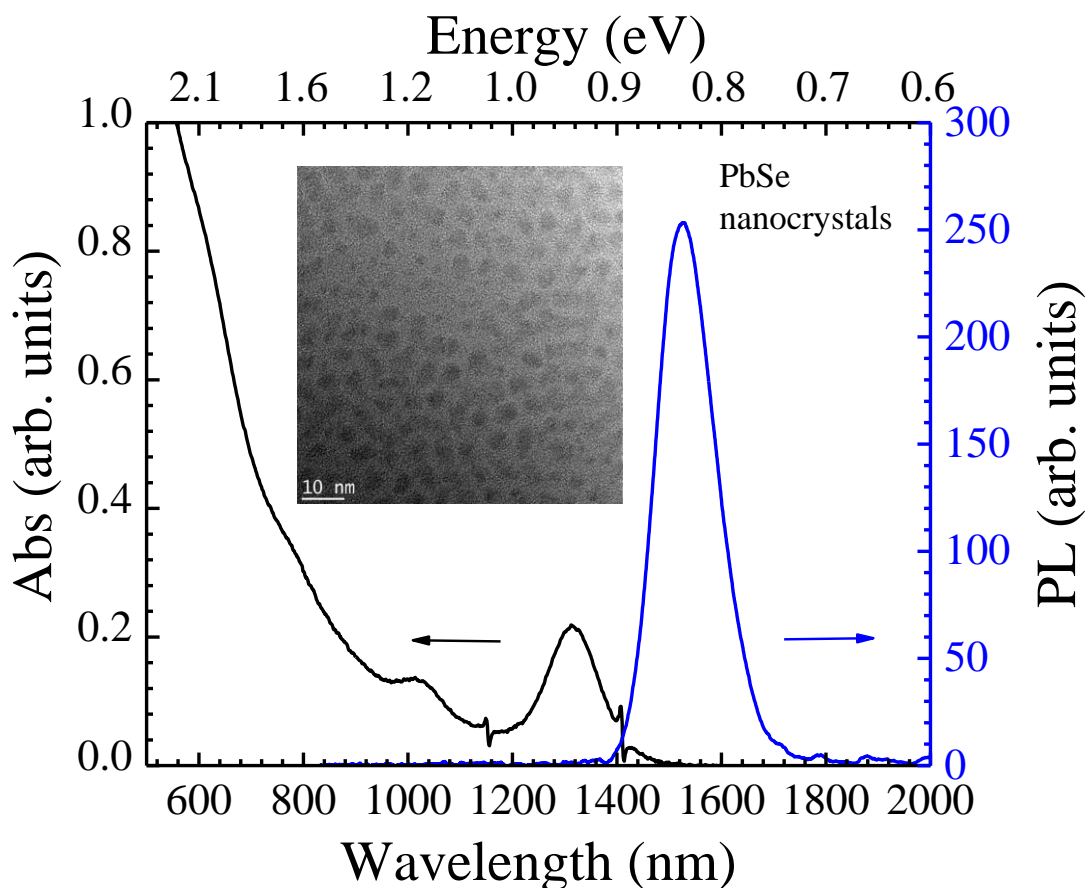


Figure 3.10. The absorbance spectrum measured at room temperature and photoluminescence spectrum measured at 77 K as a function of wavelength were obtained for PbSe nanocrystals. The inset is a TEM image.

whereas, in this work, the sample was cooled to approximately 77 K before taking measurements. The Stokes shift between the PL and absorbance spectra is approximated to be 131.9 meV. The full width at half maximum (FWHM) for the PL spectra is 71.7 meV. This sharp peak indicates a narrow size distribution in nanocrystals. The FWHM of the PL peak for PbSe is in agreement with the 105 nm found in previous research that investigated PbSe nanocrystals grown similarly [42]. The inset in Figure 3.10 is a TEM image of PbSe nanocrystals injected at 140 °C and grown for 20 seconds. The average particle size is approximately 3.242 nm and the size distribution is uniform with a standard deviation of 0.3289

nm. The quantum confinement ratio for these nanocrystals is 0.0435, which is comparable to current studies. Ratios down to 0.04 have been achieved for lead salt compounds and CdSe quantum dot studies have a reported value of 0.16 at best [35], [57].

3.2.2 PbSe/PbS

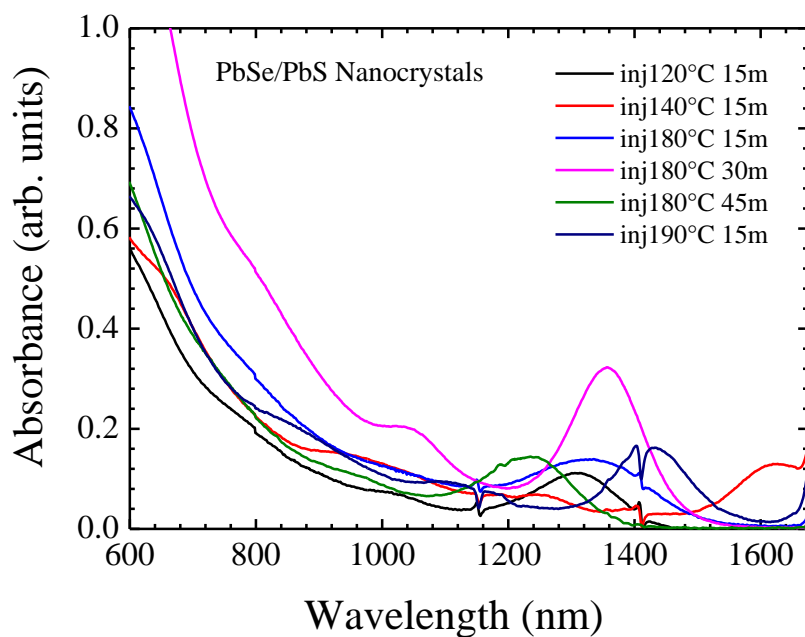
The PbSe/PbS core shell synthesis procedure was more variable than the core procedure. The PbSe nanocrystals synthesized were used in the core/shell procedure as the core compound. The procedure used was replicated from previous work [43]. However, there were issues achieving and maintaining the solution temperature outlined. Therefore, the injection temperature was inadvertently altered. Ultimately, six different combinations of growth conditions were investigated. Growth times were increased in 15 minute increments in accordance with Brumer *et al* [43], which states that each 15 minute interval results in one monolayer of growth. The absorbance spectra of these six variations are displayed in Figure 3.8 (a). Multiple excitonic transitions are visible for many of the samples. The pronounced discontinuities in the absorbance at 1152 nm and 1412 nm, again, resulted from the baseline correction.

The samples with the same injection temperature of 180 °C were isolated for clarity in Figure 3.8 (b). The onset of the absorption was used to determine the band gap of each trial. The associated band gaps for the core/shell nanocrystals grown for 15, 30 and 45 minutes are 0.821, 0.838 and 0.904 eV, respectively. Figure 3.8 (c) displays a magnified view of the first excitonic peaks for the nanocrystals with varying injection temperatures and a growth time of 15 minutes. Band gaps of 0.864, 0.698, 0.821 and 0.801 eV correspond to the samples of an

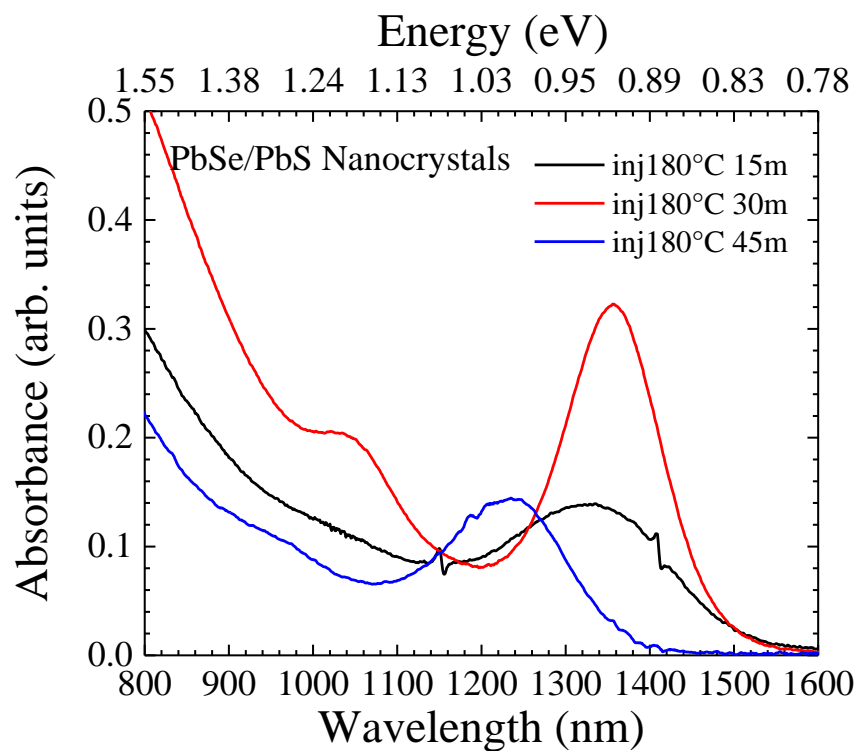
injection temperature of 120, 140, 180 and 190 °C, respectively. Saturation of the detector is visible at 1700 nm. Unfortunately, this upward trend disrupts the first excitonic peak of the sample injected at 140 °C and grown for 15 minutes. Therefore, the calculated band gap may be inaccurate.

The absorbance peaks of the spectra in Figure 3.8 (b) do not adhere to the anticipated behavior. As the injection temperature and growth time are increased, the size of the nanocrystals increases. Increased size theoretically corresponds to a decreased band gap, but this is not the behavior observed for the absorbance peaks. However, the onset of absorbance, and therefore the band gaps calculated, do follow the expected trend. In fact, as the growth time increased, the band gap increased as well. This indicates that the effective PbSe core was shrinking due to the interdiffusion of sulfur at the surface. The reduction of the PbSe coupled with the fact that PbS has a larger band gap than PbSe would lead a blue shift of the spectra to higher band gaps. The spectrum in Figure 3.8 (c) for injection at 140 °C and a growth time of 15 minutes is an outlier in that it does not adhere to the expected behavior. Possible explanations include the fact that different batches of core PbSe nanocrystals were used in each shell synthesis. The same core procedures was followed each time, but there may have been a fluctuation in size. More importantly, for the core/shell procedure, there was poor temperature control. More specifically, after the precursors were injected into the PhEt, the temperature of the solution dropped drastically. The solution was then held at the temperature at which the solution stabilized, which was inconsistent over the trials.

The core/shell nanocrystals were imaged through TEM, and are shown in Figure 3.12 (a). The average size of the core/shell nanocrystals was measured in ImageJ and was found to be 3.649 ± 0.437 nm. A zoomed in image of a singular nanocrystal is presented in Figure 3.12 (b).

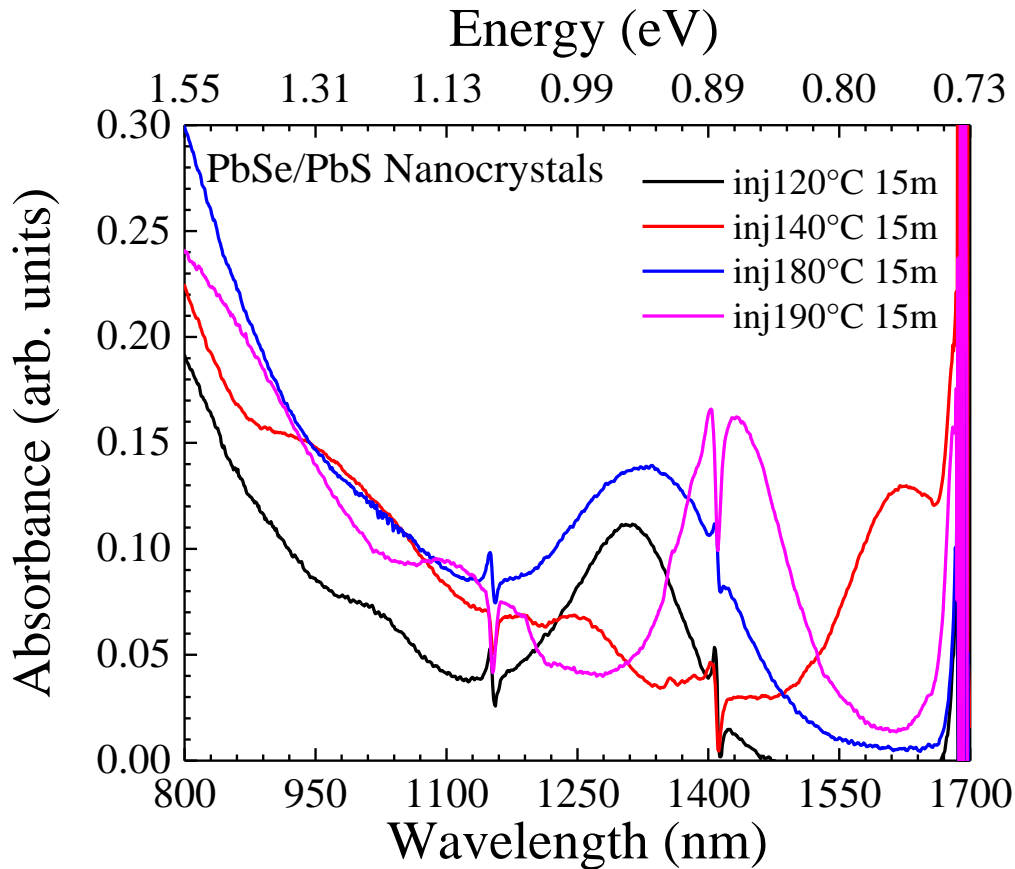


(a)



(b)

Figure 3.11. The absorbance spectra measured at room temperature as function of wavelength were obtained for PbSe/PbS nanocrystals of different sizes, as shown in (a). The spectra of the samples with differing growth times injected at 180 °C were isolated in (b).



(c)

Figure 3.11. cont'd. The spectra for nanocrystals with differing injection temperatures, all grown for 15 minutes, are plotted in (c).

The average interatomic spacing found was 3.09 \AA and is labeled. For a rock salt structure, the lattice constant is twice this spacing, 6.18 \AA . The FFT of (a) is displayed in Figure 3.12 (c), in which concentric rings associated with different interplanar spacings are visible. The primary and secondary rings have an average diameter of 11.50 and 16.69 nm^{-1} , respectively, which corresponds to an interplanar distance of 1.74 and 1.20 \AA , respectively. The FFT of a single nanocrystal is shown in Figure 3.12 (d). The cubic lattice is evident and indicates a lattice constant of 6.80 \AA .

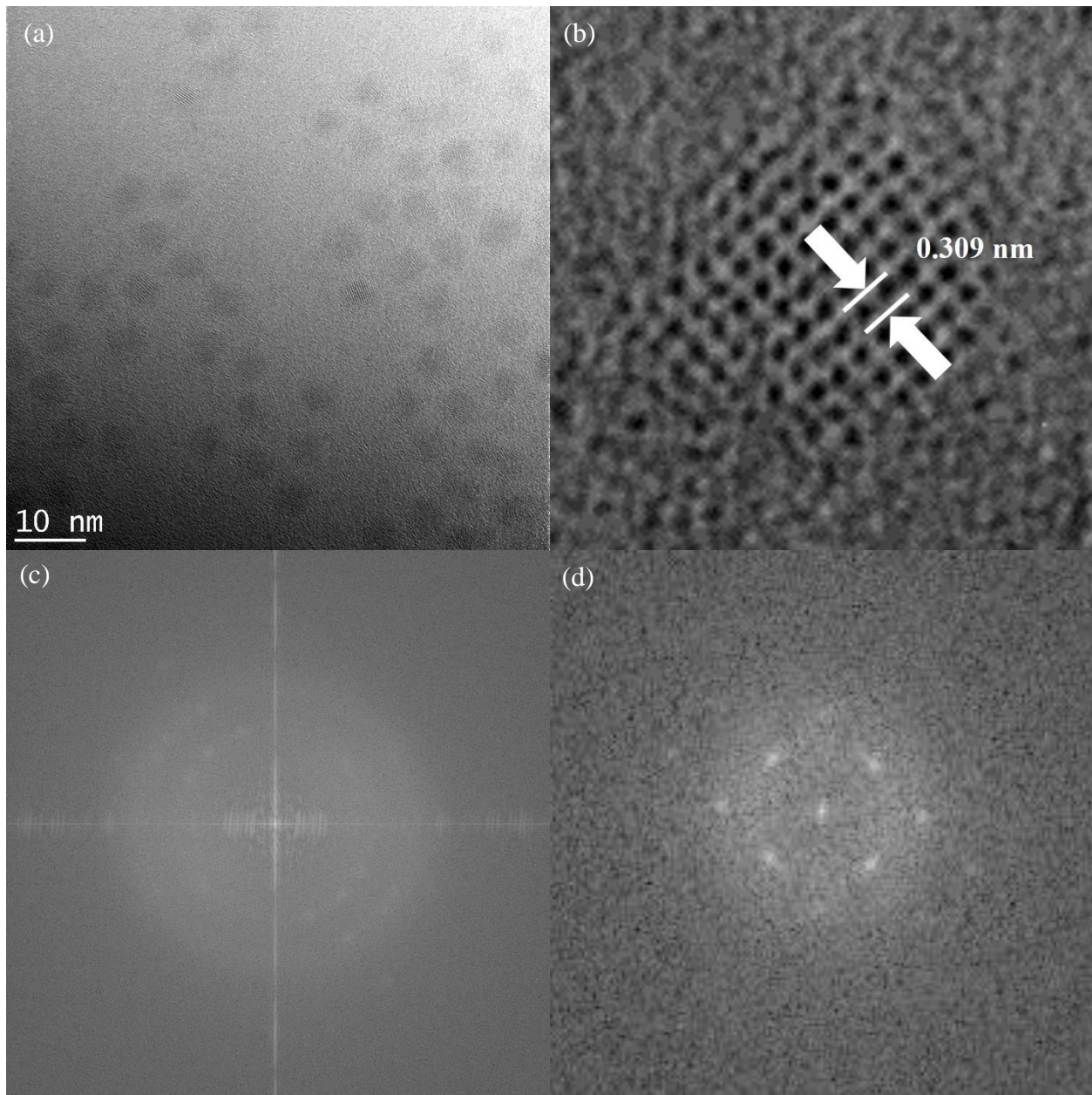


Figure 3.12. Part (a) is a TEM image of the PbSe/PbS nanocrystals grown at 180°C for 15 minutes. Image (b) is a close up of a single nanocrystal in (a), with the average measured interatomic spacing illustrated. The FFT shown in (c) is a transform of (a) . Part (d) is a FFT of image (b).

Measuring the interatomic spacing was done through analysis of the intensity variation across a nanocrystal. The total distance spanned was divided by the number of cycles, and the

interatomic spacing was 2.92 \AA . The intensity variation was plotted as a function of distance and is displayed in Figure 3.13. The inset is a close up TEM image of a single nanocrystal, as seen in Figure 3.12 (b), with the path of measurement indicated by a yellow line. By this method, the lattice constant is 5.83 \AA , which is 15% different from the lattice found through measurement of the FFT of a single nanocrystal (6.80 \AA). The lattice constant that was directly measured, 6.18 \AA , falls between these two values.

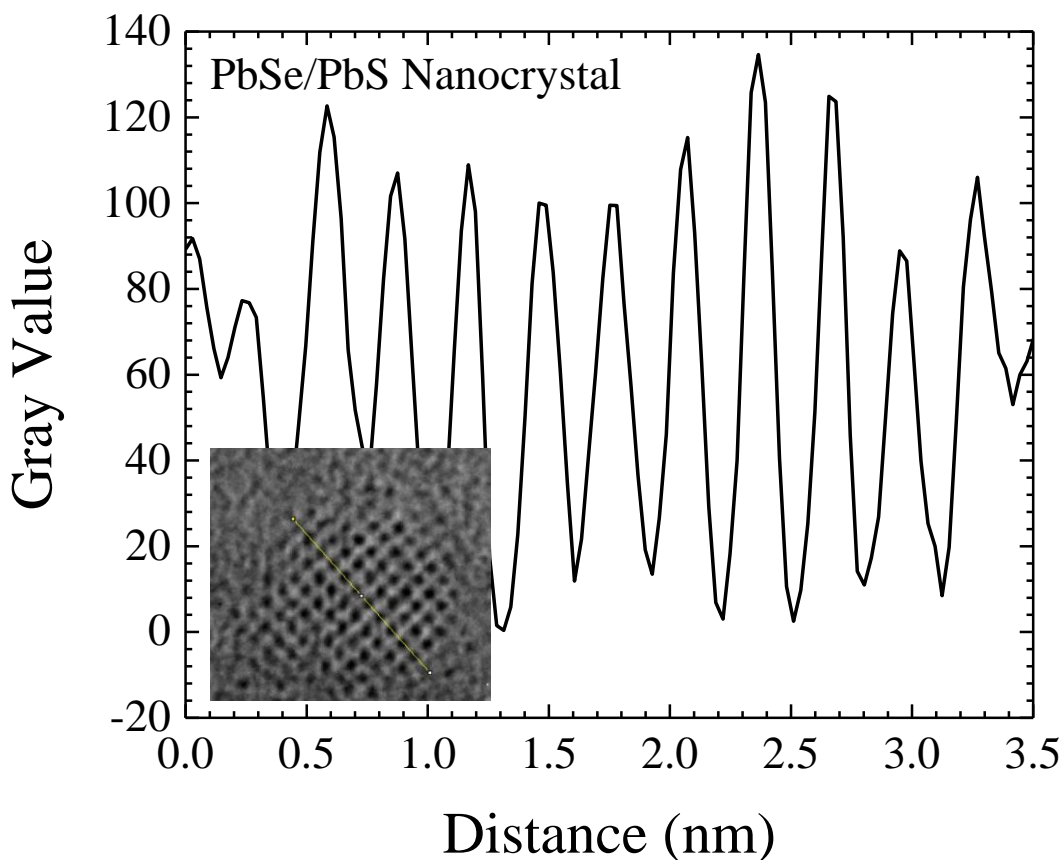


Figure 3.13. The gray value of each pixel along the yellow line seen in the inset TEM image was plotted as a function of distance.

The EDX measurement for PbSe/PbS is shown in Figure 3.14 as counts versus energy in keV. Again, carbon, copper and oxygen are present due to the method of measurement. Lead,

selenium and sulfur peaks are present and labeled, indicating that sulfur was indeed present in the nanocrystals.

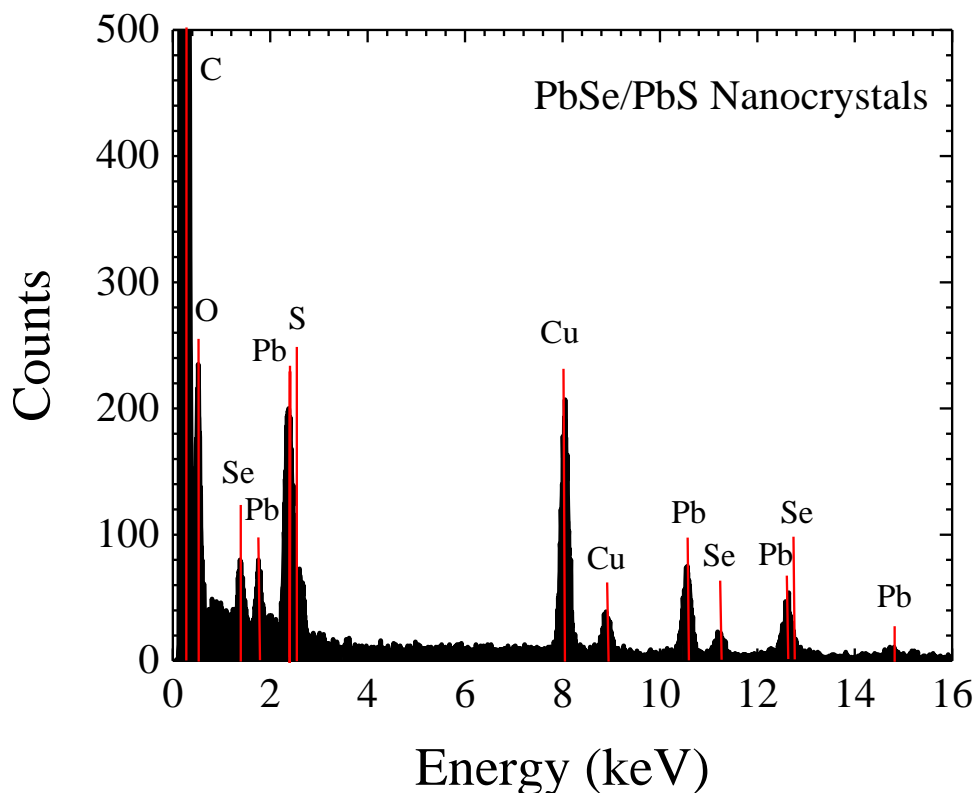


Figure 3.14. The EDX measurements of the PbSe/PbS core/shell nanocrystals are shown with each peak labeled with the corresponding element.

The absorbance and PL spectra measured at 300 K and 77 K, respectively, for the PbSe/PbS configuration are shown in Figure 3.15. The absorbance spectra exhibits a strong exciton peak for the first interband transition at 1518 nm. The secondary and tertiary interband transitions are visible at 1164 and 886 nm, respectively. There is a Stokes shift of 74.4 meV between the absorbance and emission spectra. The PL spectrum is characterized by two peaks. This indicates at least two dominant sizes of nanocrystals were synthesized. The PL peak is also wide with a FWHM of 126.4 meV, which indicates a large size distribution. This was expected

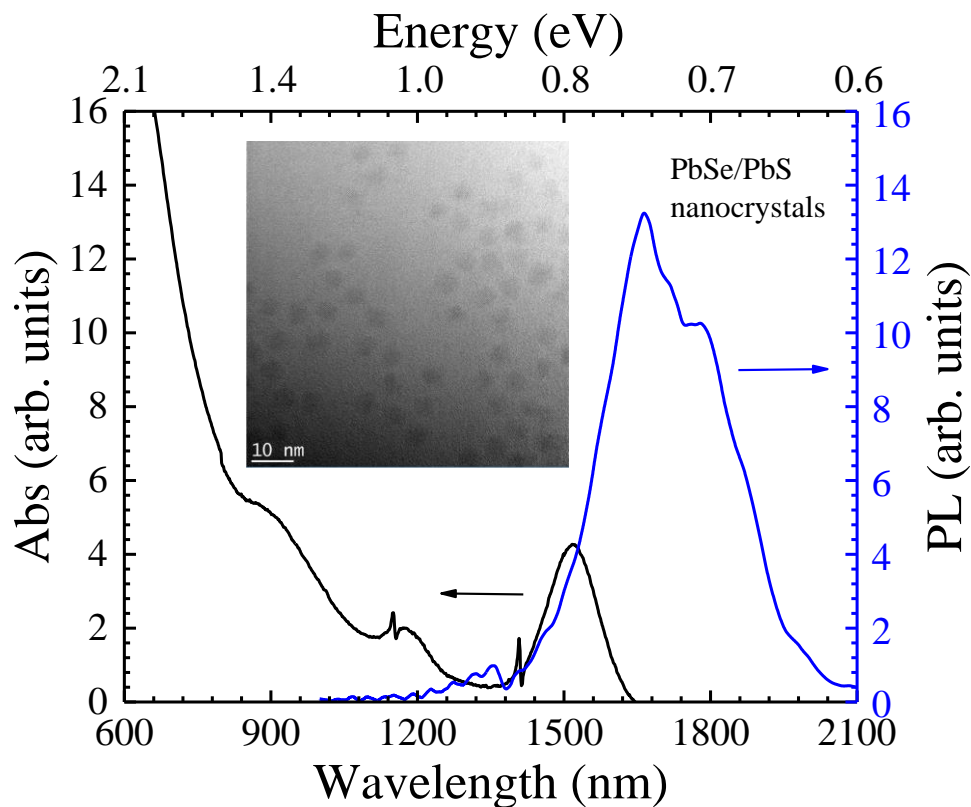


Figure 3.125. The absorbance and photoluminescence spectra as a function of wavelength for PbSe/PbS nanocrystals were measured at 300 K and 77 K, respectively. The inset is a TEM image.

because of the extended growth time of the PbSe/PbS core/shell nanocrystals. In Figure 3.15, the inset is a TEM image of the PbSe/PbS core/shell nanocrystals with an injection temperature of 180 °C and a growth time of 15 minutes with an average size of approximately 3.649 nm with a standard deviation of 0.437 nm.

The growth of a PbS shell onto the PbSe core nanocrystal does not change the cubic structure. The addition of the PbS shell on the PbSe core red shifted the PL spectra. The PL spectra for the PbSe nanocrystals contains a shoulder towards lower energy. This peak and shoulder could be explained by recombination with heavy and light holes, respectively. The FWHM for the core spectra is 71.7 meV. This small size implies a narrow size distribution.

However, the FWHM for the core/shell nanocrystals is much bigger, approximately 126.4 meV. This reflects a larger size distribution. For the PbSe/PbS core/shell nanocrystals, the PL spectrum displays multiple peaks. This may represent multiple dominant sizes of nanocrystals. The red shift of the absorption and emission spectra between the core and core/shell nanocrystals can be explained by a potential barrier induced by the shell.

3.2.3 PbSe/PbSe_xS_{1-x}

The alloy shell nanocrystals were synthesized in line with previous work [43]. However, synthesis was unsuccessful in part due to an ambiguous procedural outline. The process was repeated unsuccessfully. The absorbance spectra shown in Figure 3.16 revealed no apparent discrete transitions.

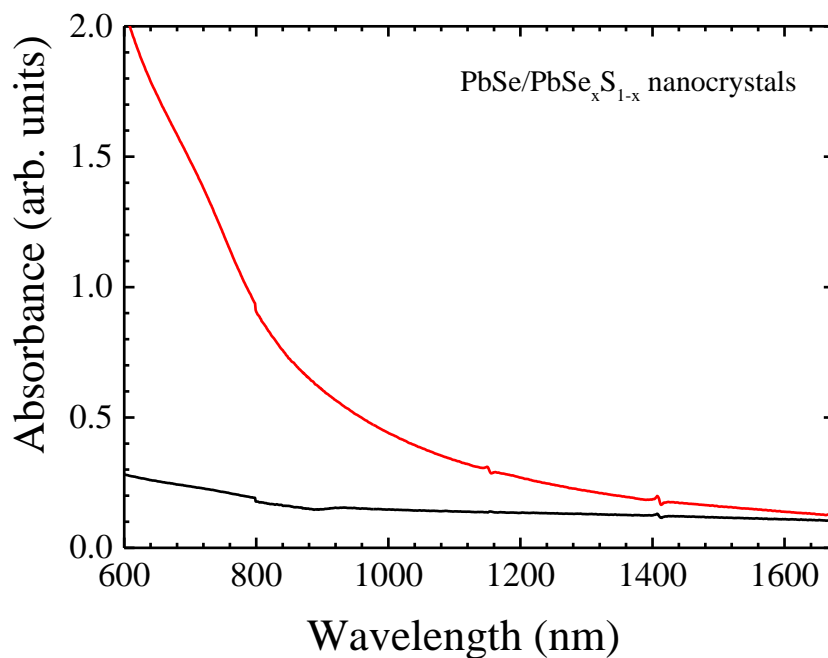


Figure 3.16. The absorbance measurement of the alloyed shell nanocrystals revealed no discrete transitions.

Chapter 4 Conclusion

Colloidally grown lead selenide and lead selenide/lead sulfide nanocrystals were characterized through absorbance, photoluminescence and TEM spectroscopy. With an increase in the growth time, the band gap of the core nanocrystals was observed to red-shift incrementally. The discretized energy levels in nanocrystals enabled fine-tuning of the band gap through size adjustment. For the PbSe core nanocrystals, the narrow PL peak and uniform TEM images indicated a small size distribution for the colloidal synthesis procedure utilized. For the PbSe/PbS nanocrystals, the size variation reflected in the TEM images and the widened FWHM of the PL spectrum increased relative to the PbSe core measurements. The increased size distribution can be attributed to an extended growth time during synthesis and an unstable temperature during growth. The absorbance and PL spectra of the PbSe/PbS nanocrystals were red-shifted relative to the PbSe core. This occurred due to a small potential barrier caused by the addition of the shell.

Bulk PbSe was simulated utilizing the LAPW method of solving density functional theory as implemented in WIEN2k. The band structure, electron density and density of states were calculated successfully. A bulk direct band gap energy of 0.4 eV and location at the L point in the Brillouin zone was correctly predicted.

References

- [1] Executive Office of the President, “THE PRESIDENT’S CLIMATE ACTION PLAN,” 2013.
- [2] M. C. Hanna and A. J. Nozik, “Solar conversion efficiency of photovoltaic and photoelectrolysis cells with carrier multiplication absorbers,” *J. Appl. Phys.*, vol. 74510, no. 100, 2006.
- [3] “National Aeronautics and Space Administration.” [Online]. Available: <https://solarsystem.nasa.gov/rps/discovery.cfm>. [Accessed: 10-Apr-2016].
- [4] W. Ma, S. L. Swisher, T. Ewers, J. Engel, V. E. Ferry, H. A. Atwater, and A. P. Alivisatos, “Photovoltaic Performance of Ultrasmall PbSe Quantum Dots,” *ACS Nano*, vol. 5, no. 10, pp. 8140–8147, 2011.
- [5] R. Vasan, Y. F. M. Makableh, J. C. Sarker, and M. O. Manasreh, “Enhanced photocurrent due to interband transitions from InAs quantum dots embedded in InGaAs quantum well solar cells,” *Mater. Res. Soc. Symp. Proc.*, vol. 1551, pp. 0–5, 2013.
- [6] E. H. Sargent, “Colloidal quantum dot solar cells,” *Nat. Photonics*, vol. 6, no. March, pp. 133–135, 2012.
- [7] A. J. Nozik, “Quantum dot solar cells,” *Phys. E Low-Dimensional Syst. Nanostructures*, vol. 14, no. 1–2, pp. 115–120, 2002.
- [8] Z. Pan, I. Mora-Seró, Q. Shen, H. Zhang, Y. Li, K. Zhao, J. Wang, X. Zhong, and J. Bisquert, “High-efficiency ‘green’ quantum dot solar cells,” *J. Am. Chem. Soc.*, vol. 136, no. 25, pp. 9203–9210, 2014.
- [9] E. H. Gong, Xiwen; Yang, Zhenyu; Walters, Grant; Comin, Riccardo; Ning, Zhijun; Beauregard, Eric; Adinolfi, Valerio; Voznyy, Oleksandr; Sargent, “Highly efficient quantum dot near-infrared light-emitting diodes,” *Nat. Photonics*, vol. 10, no. 4, pp. 253–257, 2016.
- [10] T. Ding, X. Yang, L. Bai, Y. Zhao, K. E. Fong, N. Wang, H. V. Demir, and X. W. Sun, “Colloidal quantum-dot LEDs with a solution-processed copper oxide (CuO) hole injection layer,” *Org. Electron. physics, Mater. Appl.*, vol. 26, pp. 245–250, 2015.
- [11] J. W. Stouwdam and R. a. J. Janssen, “Red, green, and blue quantum dot LEDs with solution processable ZnO nanocrystal electron injection layers,” *J. Mater. Chem.*, vol. 18, p. 1889, 2008.
- [12] M. Fardy, A. L. Hochbaum, J. Goldberger, M. M. Zhang, and P. Yang, “Synthesis and thermoelectrical characterization of lead chalcogenide nanowires,” *Adv. Mater.*, vol. 19, no. 19, pp. 3047–3051, 2007.

- [13] A. Shakouri, “Recent Developments in Semiconductor Thermoelectric Physics and Materials,” *Annu. Rev. Mater. Res.*, vol. 41, pp. 399–431, 2011.
- [14] T. C. Harman, P. J. Taylor, M. P. Walsh, and B. E. LaForge, “Quantum Dot Superlattice Thermoelectric Materials and Devices,” *Science (80-.)*, vol. 297, no. 5590, pp. 2229–2232, 2002.
- [15] B. Sothmann, R. Sánchez, and a. N. Jordan, “Thermoelectric energy harvesting with quantum dots,” *Nanotechnology*, vol. 26, no. 3, p. 32001, 2014.
- [16] Y.-J. Hung, S.-S. Hsu, Y.-T. Wang, C.-H. Chang, L.-Y. Chen, L.-Y. Su, and J.-J. Huang, “Polarization dependent solar cell conversion efficiency at oblique incident angles and the corresponding improvement using surface nanoparticle coating,” *Nanotechnology*, vol. 22, no. 48, p. 485202, 2011.
- [17] J. Han, J. Bong, T. Lim, K. H. Lee, H. Yang, and S. Ju, “Water repellent spray-type encapsulation of quantum dot light-emitting diodes using super-hydrophobic self-Assembled nanoparticles,” *Appl. Surf. Sci.*, vol. 353, pp. 338–341, 2015.
- [18] Z. I. Alexieva, Z. S. Nenova, V. S. Bakardjieva, M. M. Milanova, and H. M. Dikov, “Antireflection coatings for GaAs solar cell applications,” *J. Phys. Conf. Ser.*, vol. 223, no. May, p. 12045, 2010.
- [19] H. Peng, J.-H. Song, M. G. Kanatzidis, and A. J. Freeman, “Electronic structure and transport properties of doped PbSe,” *Phys. Rev. B*, vol. 84, no. 12, pp. 1–13, 2011.
- [20] Y. F. Makableh, “Enhancement of the Performance of GaAs based Solar Cells by using Plasmonic, Anti- Reflection Coating and Hydrophobic Effects,” University of Arkansas.
- [21] M. K. Popp, I. Oubou, C. Shepherd, Z. Nager, C. Anderson, and L. Pagliaro, “Photothermal therapy using gold nanorods and near- infrared light in a murine melanoma model increases survival and decreases tumor volume .,” *J. Nanomater.*, vol. 80301, 2014.
- [22] T. Jamieson, R. Bakhshi, D. Petrova, R. Pocock, M. Imani, and A. M. Seifalian, “Biological applications of quantum dots,” *Biomaterials*, vol. 28, pp. 4717–4732, 2007.
- [23] W. W. Yu, E. Chang, R. Drezek, and V. L. Colvin, “Water-soluble quantum dots for biomedical applications,” *Biochem. Biophys. Res. Commun.*, vol. 348, pp. 781–786, 2006.
- [24] H. M. E. Azzazy, M. M. H. Mansour, and S. C. Kazmierczak, “From diagnostics to therapy: Prospects of quantum dots,” *Clin. Biochem.*, vol. 40, no. 13, pp. 917–927, 2007.
- [25] V. Biju, S. Mundayoor, R. V. Omkumar, A. Anas, and M. Ishikawa, “Bioconjugated quantum dots for cancer research: Present status, prospects and remaining issues,” *Biotechnol. Adv.*, vol. 28, no. 2, pp. 199–213, 2010.

- [26] O. Manasreh, *Introduction to Nanomaterials and Devices*. Wiley, pp. 171-229, 2011.
- [27] G. Zaiats, D. Yanover, R. Vaxenburg, J. Tilchin, A. Sashchiuk, and E. Lifshitz, "PbSe-Based Colloidal Core/Shell Heterostructures for Optoelectronic Applications," *Materials (Basel)*, 2014.
- [28] H. N. Green, D. V. Martyshkin, C. M. Rodenburg, E. L. Rosenthal, and S. B. Mirov, "Gold nanorod bioconjugates for active tumor targeting and photothermal therapy," *J. Nanotechnol.*, vol. 2011, pp. 1–7, 2011.
- [29] J. M. Luther, M. Law, M. C. Beard, Q. Song, M. O. Reese, R. J. Ellingson, and A. J. Nozik, "Schottky solar cells based on colloidal nanocrystal films," *Nano Lett.*, vol. 8, no. 10, pp. 3488–3492, 2008.
- [30] C. C. Wang and S. Di Lin, "Resonant cavity-enhanced quantum-dot infrared photodetectors with sub-wavelength grating mirror," *J. Appl. Phys.*, vol. 113, no. 21, pp. 1–7, 2013.
- [31] X. Huang, I. H. El-Sayed, W. Qian, and M. A. El-Sayed, "Cancer cell imaging and photothermal therapy in the near-infrared region by using gold nanorods," *J. Am. Chem. Soc.*, vol. 128, no. 6, pp. 2115–2120, 2006.
- [32] P. Fomby and A. J. Cherlin, "A Near-Infrared BiFC Reporter for In Vivo Imaging of Protein-Protein Interactions," *Chem. Biol.*, vol. 72, no. 2, pp. 181–204, 2011.
- [33] E. H. Sargent, "Infrared photovoltaics made by solution processing," *Nat. Photonics*, vol. 3, no. 6, pp. 325–331, 2009.
- [34] J. B. Carruthers and J. M. Kahn, "Angle diversity for nondirected wireless infrared communication," *IEEE Trans. Commun.*, vol. 48, no. 6, pp. 960–969, 2000.
- [35] F. W. Wise, "Lead Salt Quantum Dots : the Limit of Strong Quantum Confinement," *Acc. Chem. Res.*, vol. 33, no. 1982, pp. 773–780, 2000.
- [36] H. E. Romero and M. Drndic, "Coulomb Blockade and Hopping Conduction in PbSe Quantum Dots I (pA)," *Phys. Rev. Lett.*, vol. 156801, no. 95, pp. 1–4, 2005.
- [37] O. Madelung, *Semiconductors: Data Handbook*. Springer Berlin Heidelberg, 2004.
- [38] A. C. Bartnik, F. W. Wise, A. Kigel, and E. Lifshitz, "Electronic structure of PbSePbS core-shell quantum dots," *Phys. Rev. B - Condens. Matter Mater. Phys.*, vol. 75, no. 24, pp. 1–6, 2007.
- [39] J. W. Stouwdam, J. Shan, F. C. J. M. Van Veggel, A. G. Pattantyus-abraham, and J. F. Young, "Photostability of Colloidal PbSe and PbSe / PbS Core / Shell Nanocrystals in Solution and in the Solid State," *System*, pp. 1086–1092, 2007.

- [40] I. Moreels and B. Fritzing, “Surface Chemistry of Colloidal PbSe Nanocrystals,” *J. Am. Chem. Soc.*, vol. 15081, no. 130, pp. 15081–15086, 2008.
- [41] M. H. Zarghami, Y. Liu, M. Gibbs, E. Gebremichael, C. Webster, and M. Law, “P-type PbSe and PbS quantum dot solids prepared with short-chain acids and diacids,” *ACS Nano*, vol. 4, no. 4, pp. 2475–2485, 2010.
- [42] A. Nusir, J. Aguilar, J. Hill, H. Morris, and M. O. Manasreh, “Uncooled Infrared Photodetector Utilizing PbSe Nanocrystals,” *IEEE Trans. Nanotechnol.*, vol. 15, no. 1, pp. 109–112, 2016.
- [43] M. Brumer, A. Kigel, L. Amirav, A. Sashchiuk, O. Solomesch, N. Tessler, and E. Lifshitz, “PbSe/PbS and PbSe/PbSexS1-x core/shell nanocrystals,” *Adv. Funct. Mater.*, 2005.
- [44] Varian Inc., “Cary 100/300/40/500 UV-VIS-NIR Spectrophotometer.”
- [45] M. Fox, *Optical Properties of Solids*. Oxford University Press, pp. 3-5, 2010.
- [46] ABB, “FT-IR Reference Manual,” no. August 2003, pp. 1–116, 2003.
- [47] S. Ryazantsev, R. Bergstrom, S. Prikhodko, I. Atanasov, and A. Avila-Sakar, “TITAN S / TEM (FEI), 300kV Operational Manual,” *FEI*, pp. 1–15, 2008.
- [48] NIH, “Image Processing and Analysis in Java.” 2015.
- [49] P. Blaha, K. Schwarz, G. Madsen, D. Kvasnicka, and J. Luitz, *WIEN2k: An Augmented Plan Wave Plus Local Orbitals Program for Calculating Crystal Properties*, vol. 2, pp. 7-10, 2014.
- [50] “WIEN2k.” [Online]. Available: <http://www.wien2k.at/>. [Accessed: 01-Jan-2016].
- [51] H. Eschrig, *The Fundamentals of Density Functional Theory*. .
- [52] S.-H. Wei and A. Zunger, “Electronic and structural anomalies in lead chalcogenides,” *Phys. Rev. B*, vol. 55, no. 20, pp. 13605–13610, 1997.
- [53] M. Lach-hab, D. a. Papaconstantopoulos, and M. J. Mehl, “Electronic structure calculations of lead chalcogenides PbS, PbSe, PbTe,” *J. Phys. Chem. Solids*, vol. 63, no. 5, pp. 833–841, 2002.
- [54] C. E. Ekuma, D. J. Singh, J. Moreno, and M. Jarrell, “Optical properties of PbTe and PbSe,” *Phys. Rev. B*, vol. 85205, no. 85, pp. 1–7, 2012.
- [55] A. Valdivia and G. E. Barberis, “Fully Relativistic Electronic Structure of the Semiconductors PbTe, PbSe and PbS,” *J. Phys. Chem. Solids*, vol. 56, no. 9, pp. 1141–1146, 1995.

- [56] D. Rached, M. Rabah, N. Benkhetto, M. Driz, and B. Soudini, "Calculated band structures and optical properties of lead chalcogenides PbX (X = S , Se , Te) under hydrostatic pressure," *Phys. B Condens. Matter*, vol. 337, pp. 394–403, 2003.
- [57] H. Du, C. Chen, R. Krishnan, T. D. Krauss, J. M. Harbold, F. W. Wise, M. G. Thomas, and J. Silcox, "Optical Properties of Colloidal PbSe Nanocrystals," *Nano Lett.*, vol. 2, no. 11, pp. 1321–1324, 2002.
- [58] A. M. Smith and S. Nie, "Semiconductor nanocrystals: Structure, properties, and band gap engineering," *Acc. Chem. Res.*, vol. 43, no. 2, pp. 190–200, 2010.
- [59] D. Yanover, R. Vaxenburg, J. Tilchin, A. Rubin-Brusilovski, G. Zaiats, R. K. C. Apek, A. Sashchiuk, and E. Lifshitz, "Significance of Small-Sized PbSe/PbS Core/Shell Colloidal Quantum Dots for Optoelectronic Applications," *J. Phys. Chem. C Chemistry C*, vol. 118, p. 17001–17009, 2014.
- [60] W. H. Strehlow and E. L. Cook, "Compilation of Energy Band Gaps in Elemental and Binary Compound Semiconductors and Insulators," *Journal of Physical and Chemical Reference Data*, vol. 2, no. 1, pp. 163–200, 1973.
- [61] L. Cockins, Y. Miyahara, S. D. Bennett, A. A. Clerk, S. Studenikin, P. Poole, A. Sachrajda, and P. Grutter, "Energy levels of few-electron quantum dots imaged and characterized by atomic force microscopy," *Proc. Natl. Acad. Sci. U. S. A.*, vol. 107, no. 21, pp. 9496–9501, 2010.
- [62] R. F. Egerton, *Physical Principles of Electron Microscopy*. Springer, pp. 93-115, 2005.

Appendix A: Description of Research for Popular Publication

Nanomaterials have broad applications in many important fields, such as biomedical imaging, solar cells, thermoelectric devices and light emitting diodes. Nanostructures exhibit unique properties that warrant further investigation. Both simulation and experiment are required to better understand the behavior of nanoscale materials in order to improve device functionality. Increased device efficiency and decreased cost of production are required in order for the free market to turn away from fossil fuels and take advantage of renewable energy. This is an inevitable transition due to the increasing cost of fossil fuel extraction, and awareness of the environmental damage caused by burning fossil fuels. A transition to renewable energy would create research and development jobs as well as technician positions to maintain infrastructure.

At the nanoscale, the charge carriers are spatially confined. By changing the size of nanocrystals, the properties can be adjusted to fit specific applications. This band gap engineering often leads to improvements in device efficiency because the material is tailor made to operate in its destined environment. Lead salts offer unique properties, such as large exciton Bohr radius, high dielectric constant and small effective electron and hole masses, that allow access to the extreme quantum confinement regime. This is appealing for band gap engineering and device applications.

Colloidally grown nanostructures are less expensive than vacuum-based methods which require expensive equipment and maintenance. This research developed colloidal synthesis procedures to grow PbSe and PbSe/PbS core/shell nanoparticles for photodetector applications. These nanomaterials operate within the infrared spectrum, which is important for many technological fields. Core PbSe nanocrystals of approximately 3.2 nm in diameter were synthesized using a colloidal synthesis method. The synthesis procedure resulted in uniform size

distribution and a high chemical yield. The core nanocrystals synthesized were used in the core/shell procedure as the core. The PbS shell was grown onto the core. However, the core/shell procedure had poor size distribution and chemical yield. This was likely due to poor temperature control during synthesis. The average size for the PbSe/PbS core/shell nanocrystals was 3.6 nm. The shell growth did not develop as planned. For longer growth times, or larger nanocrystals, the band gap shifted to higher energies. This is the opposite consequence expected. Therefore, it seems that during growth the PbS shell, there was significant interdiffusion at the surface. Part of the PbSe core was replaced with PbS, which has a larger band gap. The core/shell synthesis procedure was not optimal for extended growth times.

Appendix B: Executive Summary of Newly Created Intellectual Property

No new intellectual property items were created in the course of this research project. This work reported on the repeatability of synthesis procedures and the behavior of the material studied, PbSe.

Appendix C: Potential Patent and Commercialization Aspects of listed Intellectual Property Items

There were no intellectual property items listed and therefore there is no potential patents or commercialization aspects.

Appendix D: Broader Impact of Research

D.1 Applicability of Research Methods to Other Problems

The colloidal synthesis methods utilized in this research project can be used in applications other than photodetectors. Nanostructures are found in solar cells and thermoelectric devices. The lower cost and scalability of colloidal growth demonstrates a capacity for industrial use. Also, lead selenide and lead sulfide are unique materials with a large exciton Bohr radius. They have been investigated for use in thermoelectric and photovoltaic devices.

D.2 Impact of Research Results on U.S. and Global Society

While no direct impact of the research results is significant, incrementally improved photovoltaic and thermoelectric devices are important. Research that confirms or incrementally advances the knowledge of the field is important to science. Improvements in photovoltaic and thermoelectric devices are necessary to move from increasingly expensive and noxious fossil fuels to renewable energy. Harnessing solar and thermal energy is a path to increase a country's energy independence.

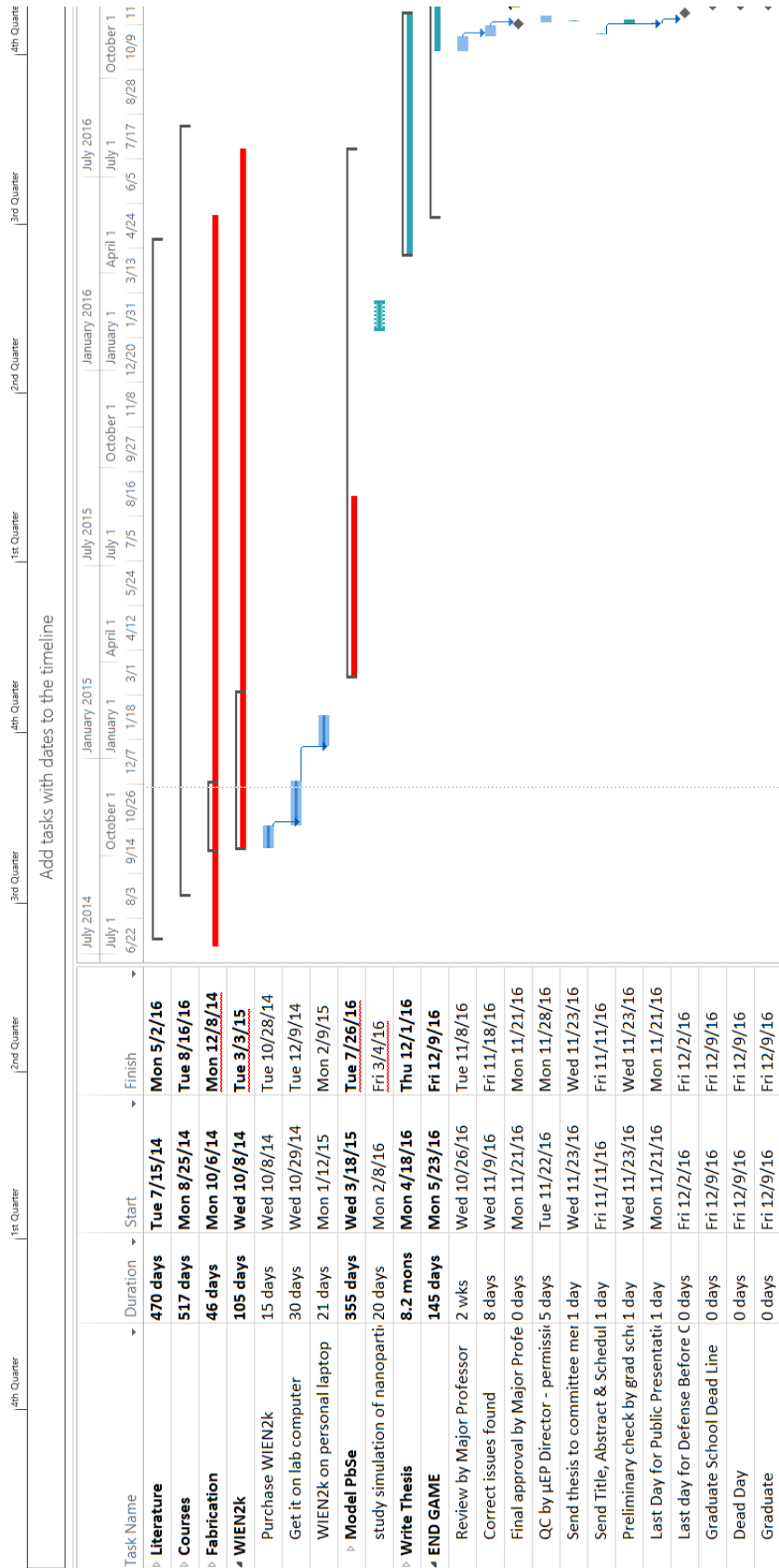
D.3 Impact of Research Results on the Environment

Improvements in devices that harness renewable energy will lead to a transition away from fossil fuels. This would have a positive impact on the environment through lower carbon

emissions and fewer damaging excavations for fossil fuels. Harvesting waste heat is possible through the use of thermoelectric devices. These can be used on cars or large-scale industrial complexes.

However, the materials studied included lead and selenium, which are toxic chemicals. Proper disposal of devices containing these materials would be a necessary challenge. Containment of the chemical in the device in all environmental conditions is the primary concern. Regulations and facilities would have to be put in place to properly recycle the devices.

Appendix E: Microsoft Project for MS MicroEP Degree Plan



Appendix F: Identification of All Software Used in Research and Thesis Generation

Computer #1:

Model Number: Q502L
Serial Number: E8N0BC041036335
Location: Personal
Owner: Haley Morris

Software #1:

Name: OriginPro Student Version
Purchased by: Haley Morris

Software #2:

Name: WIEN2k
Purchased by: Omar Manasreh

Computer #2:

Model Number: 876882794
Location: BELL 3143
Owner: Omar Manasreh

Software #1:

Name: Origin 8.6
Purchased by: Omar Manasreh

Software #2:

Name: Microsoft Office
Purchased by: Omar Manasreh

Appendix G: All Publications Published, Submitted and Planned

Published

A. Nusir, J. Aguilar, J. Hill, H. Morris, and M. O. Manasreh, “Uncooled Infrared Photodetector Utilizing PbSe Nanocrystals,” *IEEE Trans. Nanotechnol.*, vol. 15, no. 1, pp. 109–112, 2016.

Y. Makableh, A. Nusir, H. Morris, K. McKenzie, and O. Manasreh, “Performance enhancement of InAs quantum dots solar cells by using nanostructured anti-reflection coating with hydrophobic properties,” *J. Nanophotonics*. Accepted for publication on 11/29/16

Planned

H. Morris, J. Hill, J. Aguilar, A. Nusir, B. Hamad, and O. Manasreh, “Optical Properties of Lead Selenide and Lead Selenide/Lead Sulfide Nanocrystals.” . To be submitted to IEEE Transactions on Nanotechnology